

Determining the Optimal Path to Fusion at the Joint European Torus

Author:

John PATON
Amsterdam University
College (AUC)
10228918
Science Major

Supervisor:

Dr. G.M.D. HOGWEIJ
DIFFER

Co-supervisor:

Dr. F. FELICI
TU Eindhoven

Tutor:

Dr. D. VAN SCHALKWIJK

Reader:

Dr. F. BRADBURY

Capstone Thesis submitted in partial fulfillment of the requirements
for the degree of Bachelor of Science.

26-05-2014

Word count: 9537

Layman's Summary

Nuclear fusion, the joining of two atomic nuclei, may present the solution to the global energy crisis. The most promising fusion reactor design, the tokamak, induces fusion in an ionized gas (plasma) by heating it to temperatures far beyond those of the Sun. At these temperatures, the plasma has enough energy to melt any material, so it must be contained in another way: using electromagnetic (EM) fields. Since the plasma is comprised of charged particles, EM fields can be used to shape the plasma such that the hottest portion is at the centre and cooler towards the edges, allowing the containment vessel to remain intact. However, the plasma also generates its own fields, so maintaining the stability of this confinement is a challenge.

The initial heating can be accomplished in a variety of ways, adding power from different sources at different times. The precise details of the heating method can have far-reaching consequences for the duration of the plasma's confinement, so determining the best heating methods is an important step towards fusion. In this thesis, a computer model of the world's largest tokamak, the Joint European Torus, is built in a fast plasma simulation code known as RAPTOR. This model is then used as the basis for numerical optimization, a technique whereby a computer seeks out the minimum of some mathematical function. By designing a function that is minimized for various desirable plasma conditions, and which accepts the heating mechanisms as input, numerical optimization is used to find new ways to heat the plasma, resulting in better conditions for fusion. Significant improvement in the criteria examined was obtained using such an optimization technique. In the future, optimization methods may replace the current practice of simply manually selecting the heating methods based on the operator's experience.

Abstract

During the initial phase of a tokamak discharge, the current ramp-up phase, various heating systems (called actuators in the following) are used to heat the plasma and shape its profiles. The precise time evolution of these actuators – the actuator trajectories – during the ramp-up can have effects lasting long into the discharge. In this thesis, a systematic exploration of these actuator trajectories is carried out for the Joint European Torus (JET). A model of JET is first constructed using the recently developed RAPTOR (RAPid Plasma Transport simulatOR) code, incorporating JET’s primary heating actuators: ohmic heating via the plasma current, and neutral beam injection. Simulations produced by this model are found to be in good agreement with results of the more complete CRONOS suite of codes in both L-mode and H-mode.

The model is then used as the basis for a numerical optimization technique. A cost function to be minimized is designed to take as input the relevant actuator trajectories and to evaluate the plasma at the end of the simulation. Cost function terms are defined to be minimized for desirable properties, like stationarity, good confinement, and low ohmic flux consumption. Minimizing this function via numerical optimization thus amounts to seeking out trajectories which produce the best plasma as determined by the terms in the cost function. Compared to standard JET trajectories, significant improvement is observed using the optimized trajectories, even for competing goals such as stationarity and confinement. The success of the optimization warrants further investigation using more in-depth simulation software, and suggests that this kind of technique may be useful in replacing the current practice of selecting actuator trajectories based on operators’ knowledge and experience.

Keywords: tokamak, Joint European Torus, JET, plasma simulation, heating, actuator, RAPTOR, ramp-up, neutral beam injection, optimization.

Contents

Layman’s Summary	i
Abstract	ii
List of Figures	iv
List of Tables	v
Acknowledgements	vi
1 Introduction	1
1.1 The Tokamak	1
1.2 This Thesis	2
2 Background Theory	4
2.1 Tokamak Geometry and Flux Surfaces	4
2.2 Important Quantities and Profiles	7
2.3 Transport and Confinement	8
2.4 MHD and Stability	11
2.5 Important Actuators	12
2.6 Plasma Simulation and Optimization	14
3 Benchmark	16
3.1 JET Model	16
3.2 L-Mode	19
3.3 H-Mode	21
4 Optimization	23
4.1 Cost Function	23
4.1.1 Unconstrained Optimization Example	25
4.2 Constraints	27
4.2.1 Constrained Optimization Example	28
4.3 Time Knots and Sensitivity	31
4.4 Results and Discussion	32
4.4.1 Stationary State vs. s/q in H-mode	32
4.4.2 Stationary State vs. s/q in L-mode	35
5 Conclusion	38
References	40

Figures

2.1	Tokamak Geometry	5
2.2	Tokamak Coils and Magnetic Field	5
2.3	H-Mode Profiles	11
2.4	Neutral Beam Injection Direction	14
3.1	Sawtooth Transport Factors	18
3.2	NBI Density Profiles	18
3.3	L-Mode Benchmark Trajectory	19
3.4	L-Mode Benchmark Results	20
3.5	H-Mode Benchmark Trajectories	21
3.6	H-Mode Benchmark Results	22
4.1	Example Cost Function Term Contours	26
4.2	Unconstrained Optimization Example Results	26
4.3	Constraint Violation Example	28
4.4	Constrained Optimization Example Results	30
4.5	Perturbed Transport Model	32
4.6	Piecewise Nominal Trajectory Fit	33
4.7	Stationarity vs. s/q Cost Function Terms	33
4.8	Stationarity vs. s/q Optimized H-mode Profiles	34
4.9	Stationarity vs. s/q Optimized H-mode Trajectories	34
4.10	Stationarity vs. s/q Optimized H-mode NBI Configuration	34
4.11	Stationarity vs. s/q Optimized L-mode Profiles	36
4.12	Stationarity vs. s/q Optimized L-mode Trajectories	36
4.13	Stationarity vs. s/q Optimized L-mode NBI Configuration	36

Tables

3.1	JET Geometrical Properties	17
3.2	L-Mode Simulation Error	20
3.3	H-Mode Simulation Error	22
4.1	Trajectory Constraints at JET	27

Acknowledgements

I would like to thank Dick Hogewey and Federico Felici for responding to my myriad questions about plasma physics and RAPTOR, and for their encouragement and support throughout the project; the Computational Plasma Physics - High Temperature group at DIFFER for taking me on as a student; James Paton and Danu Thung for their editorial input and helpful conversations; and Forrest Bradbury for accepting the challenge of reading a thesis from outside his field.

1 Introduction

Nuclear fission, the splitting of a heavy atom, releases vast quantities of energy. This process was famously weaponized during World War II, but before long a peaceful application emerged: within only 10 years, the first nuclear power station was operating in the USSR. In present times, concerns about safety and waste management are turning public opinion against fission power. At the same time, fossil fuel supplies are being depleted at an ever-quickenening rate, and global energy usage continues to rise. Clearly, another option is necessary.

Nuclear fusion, the opposite of fission, is the joining of two lighter nuclei to form a heavier element. Like fission, fusion is highly exothermic for the right reactants, making it an enticing option for power generation. Unlike fission, however, these ‘right reactants’ for fusion are light nuclei. Since lighter elements are much more abundant than their heavier counterparts, fusion presents a long-term solution to the energy problem. The most commonly proposed reaction to fuel a power plant is the fusion of two isotopes of hydrogen, deuterium (${}^2_1\text{D}$) and tritium (${}^3_1\text{T}$), producing helium and a neutron. Deuterium is easily extracted from seawater, so its supply is almost limitless. Tritium, on the other hand, does not occur naturally on Earth. Luckily, tritium can easily be bred from lithium (which is common) by bombarding it with neutrons, which are produced in the D-T reaction. So a well-designed fusion reactor has the capacity to breed its own fuel.

1.1 The Tokamak

There are currently two main classes of fusion reactor designs: inertial confinement and magnetic confinement. Inertial confinement devices subject a small pellet of fuel to immense temperatures and pressures to induce fusion. Magnetic confinement devices use magnetic fields to trap an ionized gas, known as a plasma, as it is heated to sufficient temperatures for fusion, which are typically on the order of 100 million Kelvin. The most promising magnetic confinement reactor design is known as a tokamak. Tokamaks confine plasma inside a toroidal (doughnut-shaped) chamber. Most of the magnetic field is applied externally, but some (about 10%) is generated by electrical currents flowing through the conductive plasma.

Tokamaks operate in relatively short bursts called discharges or **shots** (see Sec. 2.2). Each shot is comprised of three phases: ramp-up, flat-top, and ramp-down. Ramp-up includes the initial heating of the plasma. During this time, the plasma current is also ramped up to its set value (typically a few MA), hence the name. During the flat-top phase, the plasma is held as close to a steady state as possible to maintain the conditions necessary for fusion. The plasma is then allowed to cool and the current is decreased in the ramp-down phase. This paper will primarily be concerned with the ramp-up.

As fusion research developed, plasma physicists began to encounter more and more instabilities. An instability is a susceptibility of a plasma to a sudden, often undesirable change in state. Controlling these instabilities is now a major component of fusion research worldwide. This puts fusion at the crossroads between plasma physics and control engineering, bringing together researchers from various disciplines for large-scale experiments.

Current plasma physics research is primarily aimed towards preparing for ITER, a massive tokamak currently under construction in France. ITER is a joint project between the EU, Japan, Russia, China, USA, India, and Korea, with the EU and Japan being the main investors. It is planned to be the first tokamak to achieve a net energy gain (more energy produced by fusion than input into the machine), with expected gains of up to ten times the input (Shimada et al., 2007). Until ITER's completion, however, the largest tokamak in the world is the Joint European Torus (JET), located near Culham, England and completed in 1983. JET consumes the equivalent of 1-2% of the UK's total power usage when in operation and has an annual budget of £60 million (EFDA, 2014a).

1.2 This Thesis

As with most tokamaks, JET is controlled by experienced operators whose role includes deciding the manner in which to heat the plasma during ramp-up. Tokamaks may employ a variety of heating mechanisms, known hereafter as actuators. The time evolution of an actuator, for example the amount of power it deposits into the plasma through time, is known as that actuator's trajectory. Currently, the operators who choose these trajectories do so based on their own experience. A more systematic approach would be desirable, but the high cost of experimenting with a wide variety of trajectories during ramp-up makes a large scale study unlikely. Plasma modelling and optimization offers an alternative.

Numerical optimization typically entails the minimizing of a function, referred to as the cost function. In very general terms, a chosen starting point is perturbed in some way. The new point is evaluated in terms of the cost function, and if

the outcome is more favourable, the optimization will continue moving in that direction, seeking the minimum of the function. It is possible to design a cost function that seeks out states of a plasma that are more favourable for fusion and stability (see Chap. 4).

In this thesis, a model is constructed of JET and benchmarked against data from existing shots. This model is then used in a numerical optimization of the actuator trajectories during ramp-up. The resulting plasma states are evaluated by cost functions that emphasize different and often competing qualities, such as temperature and plasma stability. The new, optimized trajectories may serve as a starting point for both more refined optimizations and experimental validation.

2 Background Theory

In this chapter some important background theory will be outlined, drawing heavily from Freidberg (2007) and Felici (2011). This is not intended to be extremely in-depth; rather, only the basic concepts required for this paper will be discussed, and some results will be presented without derivation. This chapter will also serve as an overview of relevant literature to the topic. First, the tokamak geometry will be described. Then important quantities and profiles will be outlined, followed by a discussion of particle transport and stability in plasmas. The relevant actuators will be described, as will the techniques of plasma simulation. Finally a brief overview will be given of the optimization technique to be employed in this paper.

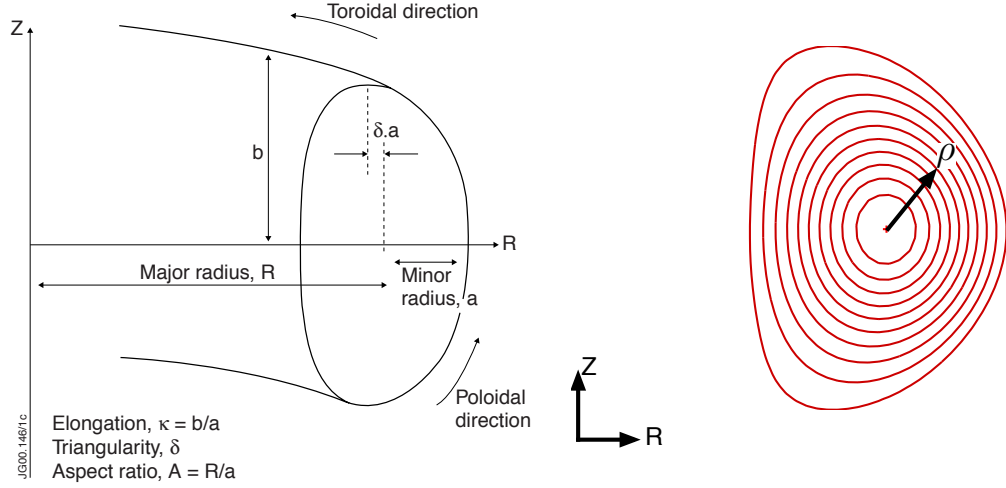
2.1 Tokamak Geometry and Flux Surfaces

The tokamak is toroidal, parameterized by the quantities in Fig. 2.1a. A cylindrical coordinate system (R, ϕ, z) is typically employed to describe 3D quantities relating the tokamak, with $\hat{\phi}$ in the toroidal direction. However, this is often not necessary due to its axisymmetry.

A tokamak confines charged particles using magnetic fields. The primary component of the magnetic field is in the toroidal direction, produced by current-carrying coils wound around the outside of the torus (see Fig. 2.2). This component directs the path of the particles around the torus. A second, smaller field component is in the poloidal direction (see Fig. 2.1a), and is generated by toroidal current flowing through the plasma. This field confines the particles radially, balancing the plasma pressure. Such a combination of fields leads to field lines which wind helically around the torus as in Fig. 2.2. This field is axisymmetric, so it is sufficient to represent it in 2 dimensions (R and z).

The poloidal flux, $\psi(R, z)$, is defined as the magnetic flux through a circular surface \mathcal{S} orthogonal to and centred on \hat{z} , of radius R , and at height z :

$$\psi(\tilde{R}, \tilde{z}) = - \int_{\mathcal{S}} \mathbf{B} \cdot d\mathbf{A} \ , \ \mathcal{S} : R \leq \tilde{R} \ , \ z = \tilde{z} \quad (2.1)$$



(a) Geometrical parameters and coordinate system displayed on a cross section of a tokamak (EURATOM & CCFE, 2013, Ch. 11). (b) A typical flux surface configuration at the TCV tokamak (Felici & Sauter, 2012).

Figure 2.1: The axisymmetry of tokamaks can be exploited to reduce the dimensionality of many quantities and equations to 2D. Flux surface averaging can further reduce to 1D.

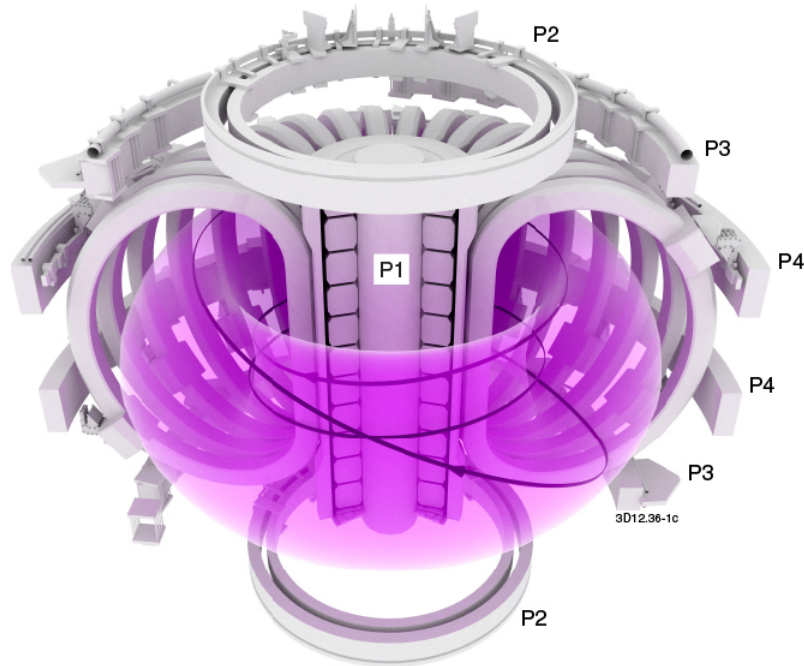


Figure 2.2: Coils carrying time-varying currents (grey bars) induce fields in the plasma (pink torus). A central solenoid (P1) induces a plasma current around the torus. Other coils (P2-P4) are used to shape the plasma. Coils wound around the torus (unlabelled) produce a toroidal magnetic field, confining the plasma. A sample helical magnetic field line with $q = 3$ is shown in deep purple (see Sec. 2.2). Image by EFDA (2014b).

with $d\mathbf{A}$ in the $+\hat{z}$ direction. Surfaces of equal ψ are known as **flux surfaces** and, in the tokamak field configuration, are typically a series of concentric ‘tubes’ extending around the torus as per the cross section in Fig. 2.1b. Note that by axisymmetry and no magnetic monopoles, $\nabla\psi \cdot \mathbf{B} = 0$, meaning all magnetic field lines must lie on these flux surfaces.

The volume enclosed by a flux surface is given by

$$V = \int dV = \int R d\phi \frac{d\psi}{|\nabla\psi|} d\ell_p = \int d\psi \oint \frac{d\ell_p}{B_p} \quad (2.2)$$

where ℓ_p is an infinitesimal length along a flux surface in the poloidal plane and B_p is the magnetic field strength in the poloidal direction (Felici, 2011).

The toroidal flux Φ is defined through a surface \mathcal{R} bounded by a poloidal flux cross-sectional ‘ring’

$$\Phi(\tilde{\psi}) = \int_{\mathcal{R}} \mathbf{B} \cdot d\mathbf{A}, \quad \mathcal{R} : \psi(R, z) \leq \tilde{\psi} \quad (2.3)$$

with $d\mathbf{A}$ now in the toroidal ($+\hat{\phi}$) direction. The toroidal flux can be used to define an **effective minor radius**, ρ :

$$\rho = \sqrt{\frac{\Phi}{\pi B_0}} \quad (2.4)$$

where B_0 is the toroidal flux at the centre of the flux surfaces, $\Phi = 0$. This effective minor radius reaches its maximum value at the edge of the plasma. For convenience, profiles in this thesis are plotted with ρ normalized to 1 at the plasma edge.

Many of the important quantities in a tokamak are constant on flux surfaces, including temperature and plasma pressure (Felici, 2011). It is thus common to represent these quantities as one dimensional spatial profiles in ρ . Profiles fluctuate in time, so it is sometimes convenient to reduce them to time traces by averaging or integrating. However, some quantities are of course not constant along a flux surface. To represent these quantities as 1D ρ profiles, they are averaged around the flux surface. For some quantity $x(R, z)$, the flux surface averaged value is given by

$$\langle x \rangle = \frac{\partial}{\partial V} \int x dV \quad (2.5)$$

2.2 Important Quantities and Profiles

The total electrical current flowing through a plasma, the **plasma current** I_p , is induced by a vertical solenoid through the middle of the torus (P1 in Fig. 2.2). This solenoid must carry a time-varying current to maintain the change in flux through the torus needed to induce the plasma current. The total change in this flux is known as the (ohmic) **flux consumption**. It can be approximated by

$$\Delta\Psi_{OH}(t) = \int_{t_0}^t V_{OH}(\tilde{t})d\tilde{t} \quad (2.6)$$

where $V_{OH}(t)$ is the induced voltage in the plasma by the solenoid and t_0 is some reference time. The current in the solenoid must constantly increase to maintain the current in the plasma. As there is a maximum to the current running in the central coil, the plasma current can only be maintained for a limited time. So after some time the plasma current must be ramped back down to zero, and the coils must cool and recharge. This is why current tokamaks must operate in shots.

Perhaps the most important profile for this project is the electron temperature, T_e . Temperatures in plasma physics are typically reported in terms of the energy (eV or keV) of the particles in question. To convert to Kelvin, one must simply make use of the Boltzmann constant in appropriate units:

$$T \text{ [K]} = \frac{T \text{ [eV]}}{k_b \text{ [eV/K]}} \approx 11\,605 \text{ K/eV} \times T \text{ [eV]} \quad (2.7)$$

The density of plasma species α (electrons, D^+ , etc.) is reported as a number density n_α , i.e. number of particles per cubic meter. The pressure of this species is defined to be

$$p_\alpha = n_\alpha T_\alpha \quad (2.8)$$

Another important profile is the **safety factor** q and its inverse, $\iota \equiv 1/q$. The safety factor is a measure of how tightly wound the helical magnetic field is around the torus. It is given by¹

$$\iota = \frac{1}{q} = \frac{\partial\Phi}{\partial\psi} = \frac{n}{m} \quad (2.9)$$

where m is the number of toroidal turns and n the number of poloidal turns made before a magnetic field line joins back to itself. A $q = 3$ line is displayed in Fig. 2.2. The safety factor is so-called because of its relation to plasma stability. In this thesis, the main concern will be that for $q < 1$, new instabilities arise (see Sec. 2.4). Small fluctuations in the $q < 1$ region may be quite important, but are

¹Note that in other conventions, the notation $\iota = 2\pi/q$ and $\bar{\iota} = \iota/2\pi = 1/q$ is often seen. This thesis will solely use the definition in Eq. (2.9).

not obvious in q profiles. However, ι is much more sensitive to these small values of q , which is why this quantity is also used in this work.

A related quantity is the **magnetic shear** s . Shear describes the degree to which magnetic field lines change their orientation from one flux surface to the next. Intuitively, a flat q profile would imply a similar magnetic field line configuration on each flux surface, so shear will be related to $\partial q / \partial \rho$. Indeed, it is defined by Felici (2011) as follows:

$$s = \frac{\rho}{q} \frac{\partial q}{\partial \rho} \quad (2.10)$$

Other common profiles include power densities for various sources and sinks, current density in the plasma, and U_{pl} , the electric potential difference around the toroidal direction. This is also known as the plasma **loop voltage**, and given by

$$U_{pl} = \frac{\partial \psi}{\partial t} \quad (2.11)$$

It can be shown that when $\partial U_{pl} / \partial \rho = 0$, the current distribution in the plasma stops evolving in time (Felici, 2011). The plasma is then said to be in a **stationary state**.

The relative error in a profile $P(\rho, t)$ with respect to some reference profile $P_r(\rho, t)$ is, in general, a function of time. In this paper, this value will be reported as a percentage and given by

$$\epsilon_P(t) = \sqrt{\frac{\sum_{\rho} [P(\rho, t) - P_r(\rho, t)]^2}{\sum_{\rho} P_r(\rho, t)^2}} \quad (2.12)$$

2.3 Transport and Confinement

Transport refers to the spatial motion of some quantity through the plasma. This may refer to the particles themselves, as well as the diffusion of heat or current. For this thesis, the most important process is heat diffusion. The diffusion is defined separately for each species in the plasma, including electrons, deuterium or tritium ions, or impurities which may be present in the plasma. If one would assume that the heat flux of species α is only driven by its own temperature gradient, and assuming a slab geometry, then the heat flux would be given by a simple equation

$$q_a = -n_a \nabla T_a \quad (2.13)$$

However, plasma transport theory predicts that the heat flux may also be driven by density gradients, temperature gradients of other species, and by the electric field.

Moreover, the tokamak geometry necessitates a geometrical correction factor. The full expression for the heat flux of species from Felici (2011) is

$$q_\alpha = -\frac{\partial V}{\partial \rho} G_1 T_\alpha n_\alpha \left[\sum_{\beta \in \text{species}} \left(\chi_{n_\beta}^\alpha \frac{1}{n_\beta} \frac{\partial n_\beta}{\partial \rho} + \chi_{T_\beta}^\alpha \frac{1}{T_\beta} \frac{\partial T_\beta}{\partial \rho} \right) + \chi_E \frac{E_{||}}{B_p} \right] \quad (2.14)$$

where n_α is the number density of α , $E_{||}$ the electric field component parallel to the magnetic field, χ_x^α represents the heat flux of α due to the gradient of the profile x , χ_E the flux due to $E_{||}$, and

$$G_1 \equiv \langle (\nabla \rho)^2 \rangle \quad (2.15)$$

Determining the coefficients χ is very challenging, since they may depend on ρ , other profiles, and each other. A variety of theoretical and empirical models for them have been proposed. This thesis will use the semi-empirical Bohm/gyro-Bohm model proposed by Erba et al. (1998) under a number of assumptions. First, heat flux of impurities will be ignored, since these constitute a small portion of the plasma. Furthermore, heat flux of the ions is unnecessary to calculate, since the ion temperature profile will be assumed to be a scaling of the electron temperature profile (see Sec. 3.1). Finally, it will be assumed that the only significant source of electron heat transport will be due to the temperature profile gradient; all other coefficients will be set to 0. It thus remains only to determine $\chi_{T_e}^e$, hereafter referred to as χ_e for simplicity.

The Bohm/gyro-Bohm model assumes that χ_e is influenced by effects at two different length scales: the minor radius a of the plasma (Bohm transport), and the normalized gyroradius $\rho^* = \rho_L/a$ (where ρ_L is the gyroradius) of the plasma ions in the magnetic field (gyro-Bohm transport). The model is presented here without derivation, but Erba et al. (1998) derived the model using dimensional analysis and expected scaling relations. In SI units, Bohm transport is described by

$$\chi_{e,b} = \frac{T_e}{e B_t} \frac{1}{L_{pe}} q^2 \quad (2.16)$$

where e is the elementary charge, B_t the magnetic field in the toroidal direction and L_{pe} the normalized pressure scale length, defined by:

$$L_x = \frac{x}{a |\nabla x|} \quad (2.17)$$

Here a is the plasma minor radius (see Fig. 2.1a).

Gyro-Bohm transport, on the other hand, is related to the ion gyroradius (Erba

et al., 1998):

$$\chi_{e,gb} = \frac{T_e}{eB_t} \frac{1}{L_{T_e}} \rho_i^* \quad (2.18)$$

$$\rho_i^* = \frac{\sqrt{m_i T_e}}{eaB_t} \quad (2.19)$$

Here m_i is the mass of the ion species in question. Note that the a dependence in L_{T_e} and ρ_i^* cancel out, leaving $\chi_{e,gb}$ independent of this length scale as desired.

Having determined the dependence on the different length scales, the electron heat transport is simply a linear combination of the two terms:

$$\chi_e = a_{e,b}\chi_{e,b} + a_{e,gb}\chi_{e,gb} \quad (2.20)$$

The coefficients have been determined empirically on a set of JET discharges. Their values for this project are discussed in Sec. 3.1.

Heat flows within the plasma, but it may also escape the plasma via thermal interaction with the walls of the containment vessel. The total amount of energy contained in the plasma is determined by applying the equipartition theorem to every particle in the plasma and integrating over the entire plasma volume:

$$W = \frac{3}{2} \langle n_{net} T \rangle V = \frac{3}{2} \langle p \rangle V \quad (2.21)$$

Here n_{net} is the total number density of the plasma. The degree to which energy is confined within a plasma is characterized by the **confinement time**, τ_E . Wesson (2004) defines this time by the simple relation

$$P_L = \frac{W}{\tau_E} \quad (2.22)$$

where P_L is the power lost by the plasma. If a plasma is held at a fixed energy using external heating sources (see Sec. 2.5) delivering a known power P_H to the plasma, then $P_H = P_L$, and $\tau_E = W/P_H$. This allows for the measurement of τ_E .

Measurements of the confinement time led to a surprising discovery in 1982: H-mode. In a review of H-mode studies in the 25 years following his discovery of the phenomenon, Wagner (2007) describes the primary feature of H-mode as an increase in confinement time by a factor of approximately 2. The term **H-mode** stands for ‘High Confinement Mode’, in contrast to **L-mode** (Low Confinement Mode), to indicate this difference. The physics governing H-mode and its causes are not well understood, but providing auxiliary power beyond a certain threshold has been observed to produce a sudden (discontinuous) increase in τ_E in what is known as the **L-H transition**.

The most important effects of entering H-mode for this project are the devel-

opment of steep gradients in the density and pressure profiles (and thus also in the plasma pressure) at the plasma edge. These gradients are brought about by a sharp reduction in χ_e in this region, known as an edge transport barrier. It is often convenient to describe this behaviour in terms of a **pedestal** of a certain height and width and as displayed in Fig. 2.3.

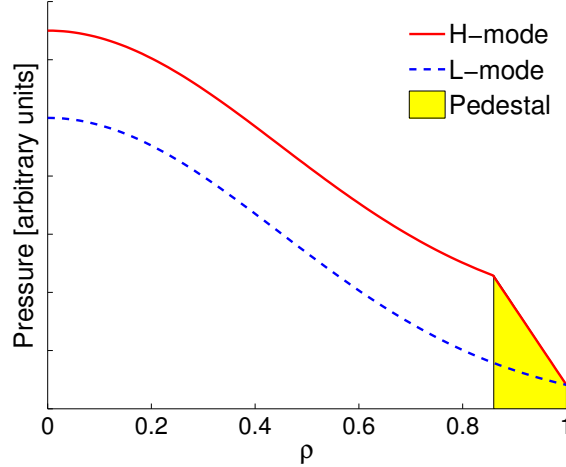


Figure 2.3: Steep gradients caused by an edge transport barrier near the plasma edge are an important effect of H-mode operation. Similar effects are observed in both the density and temperature profiles. Image adapted from FuseNet (2011). Features have been exaggerated for illustrative purposes.

2.4 MHD and Stability

Magnetohydrodynamics (MHD) is the theory of electrically conductive fluids. It combines Maxwell’s laws of electrodynamics with fluid dynamics to create a theoretical description of such a fluid. Since plasmas are fluids of charged particles, MHD is important to the study of plasma physics. MHD is mathematically complex, often requiring numerical approximations to solutions. Additionally, the details of MHD are not important to this project, only certain results. As such, MHD will primarily be addressed qualitatively. A more quantitative overview is given in Freidberg (2007).

The two most important aspects of MHD here are plasma equilibrium and stability. **Equilibrium** refers to the balance of the forces involved in confining a plasma, i.e. keeping the hot core of the plasma away from the chamber walls using some magnetic field configuration. This involves balancing the toroidal plasma’s tendency to expand along its minor radius like a hot gas (see Fig. 2.1a), but also balancing the expansion along the major radius brought about by the toroidal geometry. The precise details of the required configuration depend on the geomet-

rical properties of a given plasma. Equilibrium conditions for a given geometry may be simulated using software like CHEASE (see Sec. 2.6).

Stability refers to the degree to which a plasma tends to return to equilibrium. If a small perturbation begins to ‘roll’ away from the equilibrium position in phase space, this is a type of instability. On the other hand, if the plasma returns to its position, it is stable. Many instabilities are predicted by MHD, with stability being determined by factors including pressure, magnetic field strength, and amount of current flowing through the plasma. Avoiding these **MHD instability limits** is important to tokamak operations.

The most important instability for this work is known as the **sawtooth** instability (plural: sawteeth) or sawtooth crash. Sawteeth are so-called because of their effect on central profiles, for example temperature: the central temperature slowly builds up for some time, before suddenly crashing down, at which point the cycle begins to repeat. Sawteeth are not necessarily detrimental to tokamak operation, but they can couple to other more serious instabilities such as Edge Localized Modes and Neoclassical Tearing Modes. More detail on these instabilities and their coupling to sawteeth is provided by Hender et al. (2007). Sawteeth are associated with regions in which $q < 1$, so avoiding this condition is an important goal of this project. The sawtooth model used for this work is outlined in Sec. 3.1.

2.5 Important Actuators

The term **actuator** may refer to any quantity that can be adjusted for the tokamak, or the device that induces this desired change. The evolution through time of these quantities is known as an **actuator trajectory**. In this thesis, two important actuators will be considered: the plasma current I_p introduced in Sec. 2.2, and Neutral Beam Injection power.

The importance of the magnetic effects of the plasma current for confinement have already been discussed. However, driving a current through the plasma also has another important effect: heating. Like a current through a wire, a current through the plasma will cause the plasma to heat through its own resistivity (ohmic heating). Unlike a wire, however, the resistivity η of a plasma *decreases* with increasing temperature: $\eta \propto T^{-\frac{3}{2}}$ (Freidberg, 2007). The total power delivered to the plasma by ohmic heating is essentially given by applying Ohm’s Law at every point in space:

$$P_\Omega = \int \eta J^2 d\mathbf{r} \quad (2.23)$$

where $J = J(\mathbf{r})$ is the current density in the plasma. Since the resistivity decreases for higher temperatures, ohmic heating becomes less effective as the plasma heats.

While this does not place a firm limit on the highest possible temperature, it does make ohmic heating unattractive as the sole heating source for a fusion reactor, since extremely large currents would be required.

Neutral Beam Injection (NBI), as the name suggests, entails injecting beams of high-energy neutral atoms, typically deuterium or tritium, into the plasma. Since they are neutral, these atoms travel in straight lines until they become ionized by collisions with the plasma, at which point they are incorporated into the plasma and their energy is distributed by thermal diffusion. In this thesis it will be assumed that the neutral beam power is deposited evenly between the electrons and the ions. Strictly speaking this is untrue, but Freidberg (2007) points out that for higher density plasmas, equilibration between the electrons and ions will result in this being the net effect over long enough time scales.

The depth of neutral beam penetration into the plasma is influenced by both the plasma density and the energy of the neutral particles. Intuitively, higher energy beam particles will penetrate further into the plasma. A denser plasma will result in more frequent collisions with the beam particles, so the beam penetrates less deeply. The penetration depth of the beam determines whether the beam energy is primarily deposited near the core of the plasma or closer to the edges. Note that if the beams are too energetic or the density is too low, the beam will **shine through** the plasma and reach the opposite wall, potentially damaging the containment vessel. Thus, NBI can only be engaged under conditions that will not allow shine-through.

In this thesis, on-axis and off-axis NBI will be considered separately. The axis in question here is the magnetic axis of the plasma cross section (Fig. 2.1b), where $\rho = 0$. An **on-axis** beam crosses the magnetic axis; most of its energy is deposited at the plasma centre. Conversely, an **off-axis** beam is angled to miss the core, depositing the bulk of its energy closer to the edge of the plasma.

In addition to heating of the plasma, current can be driven using NBI by directing the beams not perpendicularly across the magnetic axis, but tangentially along it (see Fig. 2.4). Of course this requires higher energy beams as they must travel further to reach the plasma core. The degree to which injection is oriented tangentially vs. perpendicularly determines the amount of current driven.

The precise details of the NBI configuration are not important here, only the resulting power deposition and current drive profiles. The specific profiles used in this thesis are discussed in Sec. 3.1.

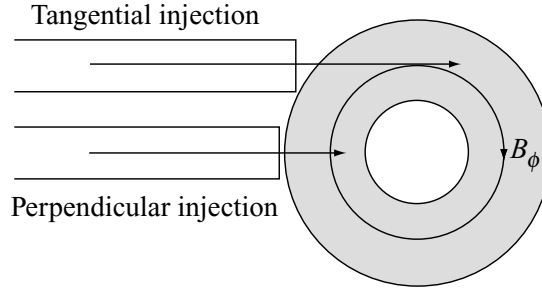


Figure 2.4: Top view of a tokamak with NBI. Injecting the beams more tangentially leads to increasing current drive (Freidberg, 2007, pp. 543).

2.6 Plasma Simulation and Optimization

Due to the high cost and complexity of plasma physics experimentation, computational models are very valuable in this field. These codes may focus on specific aspects of a plasma, or try to produce an overall simulation of a shot. They may also be interdependent, with one code using results from another.

The two main purposes of plasma simulation are interpretation of data and prediction of experimental results. Interpretation of data involves using those quantities which can be directly measured to reconstruct the plasma state during the course of a shot. Prediction, which will be the focus of this thesis, involves stipulating quantities that can be controlled before or during a shot (e.g. initial plasma conditions or actuator trajectories) and simulating the resulting plasma. Profiles such as temperature, density, and safety factor may be simulated by taking into account different transport models, heat sources and sinks, and tokamak geometry.

One example of such a code is the CRONOS suite of codes for integrated tokamak modelling (Artaud et al., 2010). CRONOS, which has both interpretative and predictive capabilities, is extensive and provides detailed simulation results. It simulates both transport and MHD equilibrium over the course of a shot. However, this depth comes at a high computational cost: simulating a single ramp-up takes about an afternoon on a standard PC. A less in-depth simulation problem is to determine the MHD equilibrium for a given configuration. The CHEASE code for toroidal MHD equilibria (Lütjens et al., 1996) has been in use for some time for this purpose.

Recently, Felici (2011) introduced a new simulation tool: RAPTOR, the RAPid Plasma Transport simulatOR. Implemented in MATLAB², RAPTOR seeks to dramatically reduce computation time while still capturing the essential physics of a tokamak shot. It accomplishes this by a combination of simplifying physical as-

²<http://www.mathworks.nl/products/matlab/>

sumptions and pre-loading the MHD equilibrium. In this way, RAPTOR depends on the output of an equilibrium simulation by a code like CHEASE, but is so fast that it is capable of simulating a shot in real-time. In fact, real-time control of tokamak plasmas was one of the main goals of RAPTOR's development. RAPTOR was also implemented with predictive capabilities. Predictive RAPTOR simulates quantities of interest on the basis of the tokamak geometry, a prescribed MHD equilibrium, a set of actuator trajectories, and the plasma initial conditions. Some plasma quantities, notably the density profile, are also prescribed for the duration of the shot.

RAPTOR's speed makes it well-suited to applications requiring multiple iterations of a simulation, including numerical optimization. It is possible to design a function to be minimized, referred to as a **cost function**, which seeks out certain plasma properties, for example high temperature. An optimization routine can then be constructed as follows. First, a set of actuator trajectories serves as the basis or **nominal case** for a plasma simulation. The results are used to evaluate the cost function. Next, the routine makes a (small) change to the set of trajectories and re-evaluates. The process iterates, subject to certain constraints, until it becomes impossible to find a lower value of the cost function, at which point the discovered trajectories are considered to optimize the function. Detailed examples are presented in Sec. 4.1 and 4.2.

The precise manner in which these steps are taken varies between different optimization algorithms. This thesis will employ the Sequential Quadratic Programming (SQP) algorithm, which permits non-linear constraints. SQP is implemented in the built-in MATLAB function `fmincon`, so the precise details are unimportant for this work (but are outlined by Nocedal (2006, Ch. 18)). Each point in time for a given trajectory is treated as a separate variable (or **free parameter**) by `fmincon`. Since increasing numbers of free parameters make the optimization more challenging, optimizing the trajectory at all available times for even one actuator is unfeasible. Instead, a selection of time points (or **time knots**) are taken as the free parameters, and the rest of the trajectory is interpolated in some way between these points, allowing for e.g. a piecewise constant or piecewise linear definition of the trajectory.

Since RAPTOR was developed so recently, and since other codes are so computationally intensive, little work has been performed using automated optimization techniques for actuator trajectory modelling. Notable exceptions include the proof-of-concept for such optimization in Felici (2011) for the TCV tokamak in Lausanne, and an optimization of simulated ramp-ups for ITER by Van Dongen (2013).

3 Benchmark

The benchmarking process entails specifying actuator trajectories (and other shot-specific quantities) which fit a certain shot, and comparing the results to (interpreted) experimental data or to other predictive simulations to determine the accuracy of the model. Confirmation of the model’s capabilities to reproduce experimental data is vital before meaningful optimization can take place. The first section of this chapter will outline the various machine-specific features of JET that were implemented into RAPTOR.

Next, the benchmarking against two specific shots¹, one remaining in L-mode and one entering H-mode, will be presented. This will include reporting the actuator trajectories and other shot-specific quantities, and evaluating the results to determine the usefulness of an optimization based on this model. The JET data used is a combination of measured data and interpretation by CRONOS (Artaud et al., 2010), but will hereafter simply be referred to as ‘the data’ except where the distinction is important. Note that the actuator trajectories presented here will partially be used as the nominal case for the optimization in Chap. 4. In this chapter, ρ will be normalized unless otherwise stated.

3.1 JET Model

The geometrical quantities as per Fig. 2.1a are outlined in Tab. 3.1. Alpha particle heating is assumed to be negligible, as are power losses due to radiation of accelerating charges. Electron-ion thermalization is modelled by assuming the ion temperature is a scaling of the electron temperature, with the scaling factor increasing linearly to 1 at the plasma edge. The central scaling factor may also evolve in time:

$$T_i(\rho, t) = c_T(\rho, t)T_e(\rho, t) , \quad c_T(\rho, t) = c_{0,T}(t)(1 - \rho) + \rho \quad (3.1)$$

¹The JET data used in this and all following sections was made available by DIFFER.

Quantity	Symbol	Value
Major Radius	R	2.88 m
Minor Radius	a	1.25 m
‘Vertical Radius’	b	2.10 m
Elongation	κ	1.68
Triangularity	δ	0.3
Aspect Ratio	A	2.3

Table 3.1: Values of the geometrical quantities in Fig. 2.1a for JET.

For each shot, the edge ($\rho = 1$) temperature was held fixed at 50 keV. The initial temperature profile was assumed to be a gaussian of the form

$$T_{e,initial}(\rho) = T_{0,initial} \exp\left(-\frac{\rho^2}{w_t}\right) \quad (3.2)$$

where $T_{0,initial} = 0.8$ keV and $w_t = 0.6$.

The transport model used was the semi-empirical Bohm/gyro-Bohm model (see Eq. (2.20)), with coefficients of $a_{e,b} = 8 \times 10^{-5}$ and $a_{e,gb} = 7 \times 10^{-2}$. These coefficients have been adapted from Erba et al. (1997), with $a_{e,gb}$ having been increased by a factor of 2 from Erba’s results in keeping with the CRONOS code.

Sawteeth are modelled ‘continuously’ in RAPTOR: thermal diffusivity is increased ($\chi \rightarrow c_\chi \chi$) and conductivity is decreased ($\sigma \rightarrow c_\sigma \sigma$) by a factor at each point in ρ based on q at that point:

$$c_\chi(q) = \frac{c_{0,\chi}}{1 + \exp\left(\frac{q-0.95}{w_\chi}\right)} + 1 \quad (3.3)$$

$$c_\sigma(q) = \frac{c_{0,\sigma}}{1 + \exp\left(-\frac{q-0.95}{w_\sigma}\right)} + 1 - c_{0,\sigma} \quad (3.4)$$

These correction factors give the greatest sawtooth effect at the point where q is lowest, and have an effective width, w . Sawtooth activity can thus be simulated without computing the crashes explicitly. Sawteeth were modelled in this paper with $c_{0,\chi} = 8$ and $w_\chi = 0.2$ for diffusivity, and $c_{0,\sigma} = 1$ and $w_\sigma = 0.03$ for conductivity, resulting in factors which are displayed graphically in Fig. 3.1.

JET’s neutral beam injection systems were modelled as one on-axis and one off-axis injection box. On-axis here implies power deposition concentrated near $\rho = 0$, whereas off-axis power is deposited further towards the plasma edge. Each NBI module was also modelled as driving a fairly weak current. The power and current drive density profiles used are displayed in Fig. 3.2. On- and off-axis power trajectories could be set independently of each other. The plasma current trajectory is simply prescribed in RAPTOR.

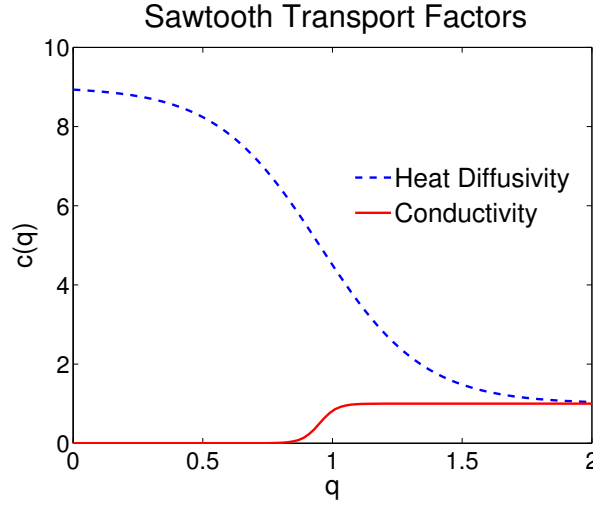


Figure 3.1: Eq. (3.3) and (3.4) with the parameter values given in-text. The most significant sawtooth corrections are at low q , whereas the effects are negligible for high q , corresponding to the overall effects of sawtooth crashes.

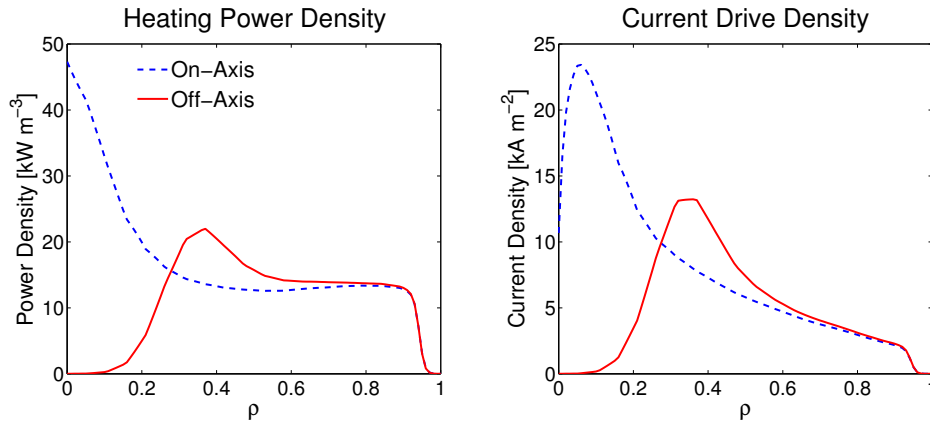


Figure 3.2: NBI density profiles for on- and off-axis modules. Note that both the on- and off-axis power densities integrate to 1 MW over the entire torus. This is not the case for the current drive profiles, which are scaled to match experimental observations.

3.2 L-Mode

JET shot 83223 was used for the L-mode benchmark. The simulation was run from 1.5 s to 11.9 s after plasma breakdown (the time at which the gas becomes ionized). During the period in which the data was collected for both this shot and the H-mode shot, there was an issue with a detector at JET which made measurement of the ion temperature impossible. It is for this reason that T_i was simply taken to be the rescaling of T_e given in Eq. (3.1), with $c_{0,T} = 0.82$ for all t . Furthermore, several profiles were prescribed to perfectly correspond to the shot in question; these were the electron and ion densities, and the effective charge, which is a measure of the impurities in a plasma.

The simulation results are displayed in Fig. 3.4. Note that in calculating the error in U_{pl} , only the data for $\rho < 0.9$ was taken into account due to observed erratic behaviour near the plasma edge in the CRONOS output. Visual inspection reveals good agreement between the T_e and q profiles, however U_{pl} is observed to deviate significantly after the end of the ramp-up, with its profile flattening while the CRONOS profile retains its shape.

A quantitative summary of the simulation error is provided in Tab. 3.2. The electron temperature and the safety factor have both low average errors which do not deviate strongly in time, though one unexplained peak in ϵ_{T_e} does occur at 2.1 s. However, the plasma loop voltage deviates significantly more from the CRONOS output, especially after the end of the ramp-up at 8.0 s. The flattening of the RAPTOR profile is in fact to be expected at the end of the ramp-up, which is when a more stationary state (and therefore a flat U_{pl} profile) typically develops. The reason for the CRONOS profile's retention of its shape is not entirely clear, but appears to be an error in CRONOS's handling of sawteeth (G.M.D. Hogeweij, private communication, March 17, 2014). Since RAPTOR behaves as expected, the profile is assumed to be fairly accurate, though this cannot be quantified. It is thus concluded that a meaningful optimization of the I_p trajectory can be performed on the basis of this model.

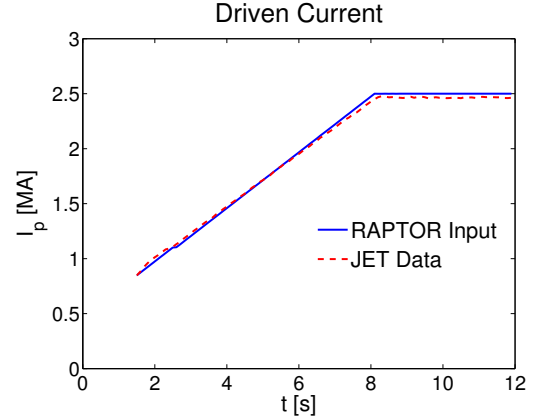


Figure 3.3: The only actuator trajectory for the L-mode benchmark. The plasma current is steadily ramped up from 0.8 MA to its maximum of 2.5 MA, which it reaches at $t = 8.0$ s.

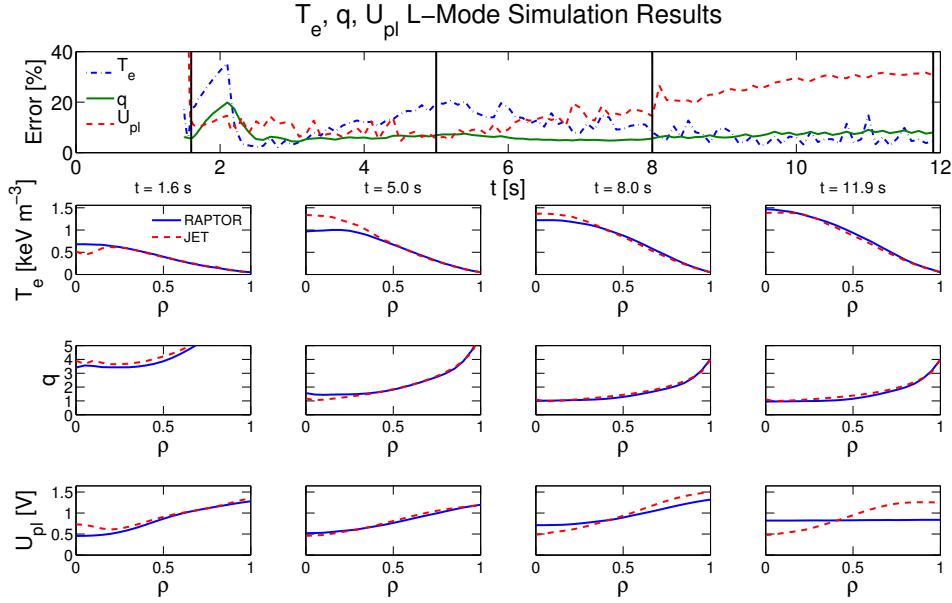


Figure 3.4: **Top row:** Time evolution of profile error in T_e , q , and U_{pl} . **Below:** Simulated profiles are displayed after initial transient behaviour ($t = 1.6$ s), midway through current ramp-up (5.0 s), at end of ramp-up (8.0 s) and at end of simulation (11.9 s). Displayed times are indicated by black bars above.

Profile	$\langle \epsilon \rangle_t$ (%)	Std. Dev. (%)
T_e	5.8	5.3
q	3.9	2.7
U_{pl}	9.6	10.5

Table 3.2: Time-averaged profile error and standard deviation of the error for the profiles in Fig. 3.4. All quantities calculated excluding initial transients (first 0.1 s of simulation).

3.3 H-Mode

The H-mode simulation was benchmarked against JET shot 83224, which utilized both Ohmic heating and NBI. Plasma was simulated from 1.5 s to 12.0 s after breakdown. The I_p trajectory was the same as for shot 83223 (see Fig. 3.3), and the NBI trajectories are given in Fig. 3.5. The proportion of on- to off-axis power was determined by performing a least-squares fitting of the two NBI power density profiles in Fig. 3.2 to the power deposition profile from the data at each time step. The transition to H-mode was at 4.0 s, at the time when NBI power was engaged. The edge of the pedestal was placed at 0.4 keV and $\rho = 0.93$. Electron-ion

thermalization was modelled with $c_{0,T} = 0.80$ before the L-H transition at 4.0 s, and $c_{0,T} = 0.97$ thereafter (see Eq. (3.1)). As with the previous shot, the electron and ion density and the effective charge profiles were set to match JET.

Results of the simulation are displayed in Fig. 3.6. Again, only $U_{pl}(\rho < 0.9)$ was considered for error calculations due to erratic behaviour in CRONOS. Visual inspection reveals the central ($\rho = 0$) electron temperature to be consistently low, but the remainder of the profile appears to agree well, including the pedestal. One large peak in ϵ_{T_e} is observed at 11.1 s, coinciding with the last large step in NBI power. Such a peak was also observed in $\epsilon_{U_{pl}}$, but at 4.0 s, again at a large NBI power step. This merely suggests a slight mismatch between the response times of CRONOS and RAPTOR to these large steps, not a major deviation from the actual situation inside JET. A more concerning peak is the rise in ϵ_{T_e} after $t = 11.0$ s. Similarly to Sec. 3.2, RAPTOR's U_{pl} profile is again observed to flatten further than that of CRONOS, which is again likely a result of a sawtooth handling issue in CRONOS.

The simulation error is quantitatively summarized in Tab. 3.3. Overall the errors and spreads are comparable to those of the L-mode shot (Tab. 3.2), despite the large and sudden changes in NBI power and the operation in H-mode. This lends additional confidence to the quality of the NBI and H-mode simulation in RAPTOR. The increasing error in T_e after $t = 11.0$ s was sufficient cause for concern

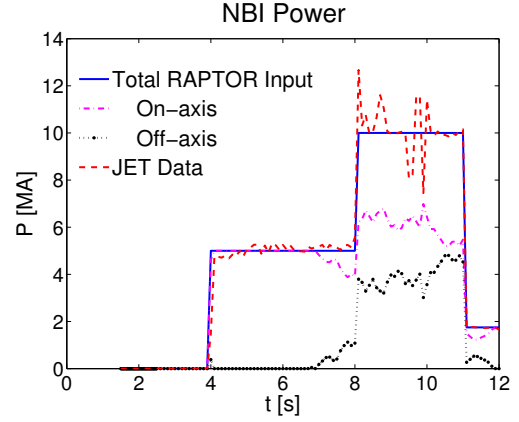


Figure 3.5: NBI trajectories for the H-mode benchmark. The total NBI power is first stepped to 5 MW at $t = 4.0$ s and then to 10 MW at 8.0 s, and finally to 1.75 MW at 11.0 s. The individual on- and off-axis trajectories sum to match the JET data. See Fig. 3.3 for plasma current trajectory.

to remove this segment from the optimization, such that optimization results were only for the most reliable time period. It is thus concluded that optimization of I_p and both NBI power trajectories may be meaningfully performed for $t \leq 11.0$ s using this model.

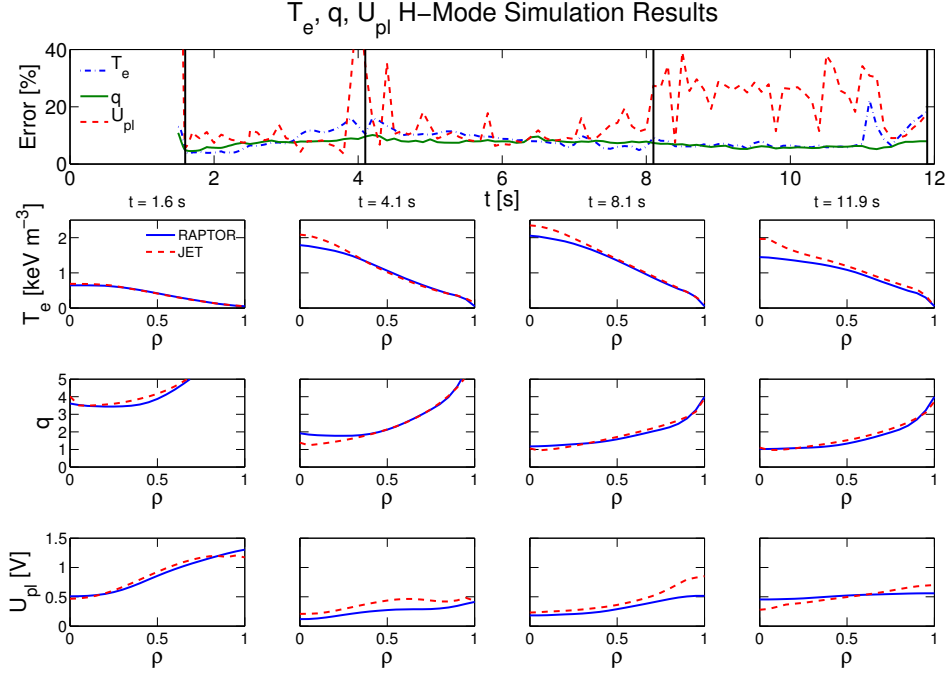


Figure 3.6: **Top row:** Time evolution of profile error in T_e , q , and U_{pl} . Note that one peak in $\epsilon_{U_{pl}}$ was excluded to ease readability: 59.6 % at 4.0 s. **Below:** Simulated profiles are displayed after initial transient behaviour ($t = 1.6$ s), after first NBI power step (4.0 s, see Fig. 3.5), after second step (8.0 s) and at end of simulation (11.9 s). Displayed times are indicated by black bars above.

Profile	$\langle \epsilon \rangle_t$ (%)	Std. Dev. (%)
T_e	4.7	4.8
q	4.0	3.5
U_{pl}	9.1	10.9

Table 3.3: Time-averaged profile error and standard deviation of the error for the profiles in Fig. 3.4. All quantities calculated excluding initial transients (first 0.1 s of simulation).

4 Optimization

In this chapter, the RAPTOR models presented in Chap. 3 will be numerically optimized in search of new actuator trajectories. First, the composition of the cost-function will be explored, followed by a simple illustrative optimization example. Next, constraints will be introduced and their effects discussed. Finally, a full optimization of the JET ramp-up in both H-mode and L-mode will be presented.

4.1 Cost Function

The cost function J is composed of a number of terms which are minimized when different criteria are met. These terms have been previously defined by Felici (2011) and Van Dongen (2013), but most are intuitive enough to be presented without in-depth explanation. Cost function terms are typically defined by a weighted norm function given by

$$||f||_W^2 \equiv \int_0^{\rho_{max}} [W(\rho)f(\rho)]^2 d\rho \quad (4.1)$$

Here $f(\rho)$ describes the penalization for deviation from the desired characteristic, and $W(\rho)$ is a weight function which may be used to emphasize certain areas in ρ , e.g. increasing importance towards the centre. Most often this is not necessary, in which case $W(\rho) = 1$. This will be assumed in this chapter unless explicitly stated otherwise.

The first desirable characteristic is **stationarity** (where the current-distribution ceases to evolve in time) at the end of the ramp-up (t_f). A plasma is in a stationary state when $\partial U_{pl}/\partial \rho = 0$: a flat profile. Van Dongen (2013) found that simply penalizing this derivative led to profiles which came close to a stationary state, but required a long time to fully reach it, which is unfavourable given the limited timeframe of a shot. Instead, he demonstrated that the term

$$J_{ss} = ||\sigma_{||} [U_{pl}(t_f, \rho) - U_{pl}(t_f, \rho_{max})]||_{W_{ss}}^2 \quad (4.2)$$

avoided this issue. Here $\sigma_{||}$ is the conductivity of the plasma for currents parallel to the magnetic field.

A more stringent characteristic is the **steady-state**, which could in theory permit continuous operation to replace shots (Freidberg, 2007). This state is achieved when the entire U_{pl} profile is zero, again at the end of the ramp-up. Thus the loop-voltage itself is simply penalized:

$$J_{U_{pl}} = \|U_{pl}(t_f, \rho)\|_{W_{U_{pl}}}^2 \quad (4.3)$$

As an alternative to full steady-state operation, the flat-top phase can be extended by reducing the load on the external coils used to drive the plasma current. This is achieved by minimizing the flux consumed during the ramp-up

$$J_{\Psi_{OH}} = \Delta\Psi_{OH}^2(t_f) \quad (4.4)$$

with $\Delta\Psi_{OH}(t)$ defined as in Eq. (2.6).

One final term involves the ratio of the of magnetic shear to safety factor, s/q , as follows. A type of turbulence known as Ion Temperature Gradient (ITG) turbulence prevents the normalized ion temperature gradient, $|\nabla T_i|/T_i$, from increasing beyond a certain threshold. It is preferable to increase this threshold near the edge of the plasma so that T_i can increase more sharply near the edge, allowing more energy to be confined within the bulk of the plasma. Citrin et al. (2010) demonstrated that since $|\nabla T_i|/T_i \sim 1 + s/q$, and since the outer region of the plasma contributes more to volume integrals, maximizing the volume averaged s/q (or, equivalently, minimizing $-s/q$) implies a high ITG turbulence threshold near the edge and therefore improved confinement. Van Dongen (2013) thus defines the term to minimize as

$$J_{s/q} = -\int \frac{s}{q} dV = -\int \frac{\partial V}{\partial \rho} \frac{s}{q} d\rho \quad (4.5)$$

The second definition including $\partial V/\partial \rho$ is useful since profiles are generally functions of ρ and $\partial V/\partial \rho$ is output by RAPTOR predictive simulations. This term is minimized for low, broad q profiles which rise sharply near the plasma edge.

With these different terms defined, an overall cost function can be constructed with relative weights ν given to each term:

$$J = \nu_{U_{pl}} J_{U_{pl}} + \nu_{ss} J_{ss} + \nu_{\Psi_{OH}} J_{\Psi_{OH}} + \nu_{s/q} J_{s/q} + \dots \quad (4.6)$$

Clearly this cost function generalizes simply by adding other terms. Note that the J_i are not, in general, of the same order of magnitude, so the ν_i must be chosen wisely to produce the desired relative importance in the cost function.

4.1.1 Unconstrained Optimization Example

To demonstrate the behaviour of the cost function and the search for a minimum, a simple unconstrained example will be presented. The trajectory will be based on Fig. 3.3, and the L-mode model will be used (Sec. 3.2). The plasma current will be fixed at the initial and final time, parameterized by two time knots ($t_1 = 4.0$ s and $t_2 = 8.0$ s), and interpolated linearly between the knots. The trajectory is thus specified by

$$p = [0.85 \text{ MA}, I_{p1}, I_{p2}, 2.5 \text{ MA}]^T \quad (4.7)$$

corresponding to time knots of 1.5 s, 4.0 s, 8.0 s, and 12.0 s.

The cost function will consider only $J_{U_{pl}}$ and $J_{\Psi_{OH}}$:

$$J = J_{\Psi_{OH}} + \nu_{U_{pl}} J_{U_{pl}} \quad (4.8)$$

Note that only one weight ν is needed since only the relative sizes of the terms is of consequence. Since there are only two changing parameters involved, it is possible to simply scan the parameter space within a certain region and examine the properties of the cost function and its terms there.

Contour plots of the two terms are displayed in Fig. 4.1. From visual inspection, $J_{U_{pl}}$ appears to be largely insensitive to I_p at t_1 (I_{p1}), but favours high current at t_2 (I_{p2}). $J_{\Psi_{OH}}$ seems to be minimized for high I_{p1} and $I_{p2} \approx 2$ MA. Summing these two terms will clearly yield a minimum with high I_{p1} , but the value of I_{p2} will be strongly influenced by the choice of $\nu_{U_{pl}}$. In particular, for increasing importance of $J_{U_{pl}}$, we expect increasing I_{p2} and slightly decreasing I_{p1} induced by the edge of the explorable parameter space.

Performing optimizations for values of $\nu_{U_{pl}}$ ranging from 0 (no importance of $J_{U_{pl}}$) to 1000 (high importance) yields the optimal points in Fig. 4.2. All of these points used the nominal trajectory of Fig. 3.3. The expected behaviour is observed: I_{p2} rises with increasing emphasis on $J_{U_{pl}}$, while I_{p1} decreases to avoid the inaccessible region. Visual inspection confirms that the $\nu_{U_{pl}} = 0$ point indeed corresponds to the minimum of the $J_{\Psi_{OH}}$ contour, further suggesting that the optimization routine is behaving as expected.

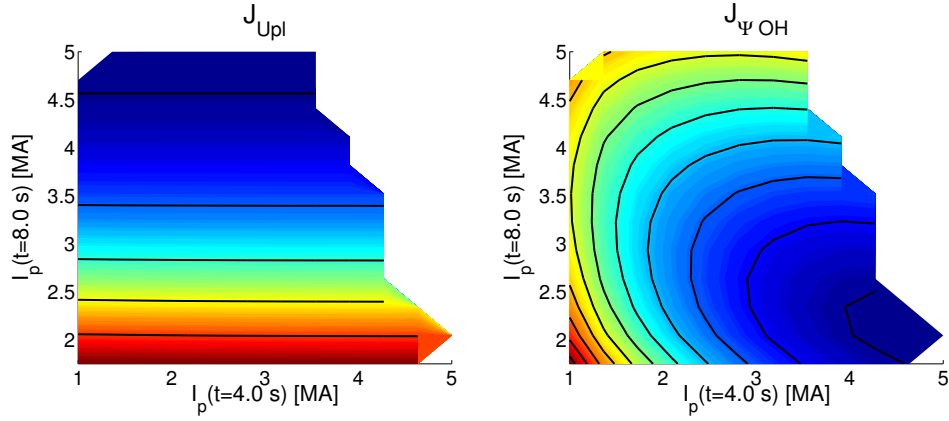
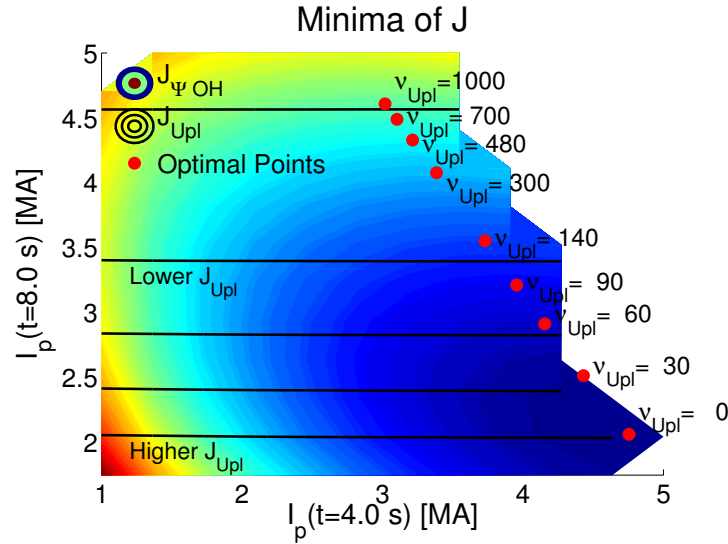
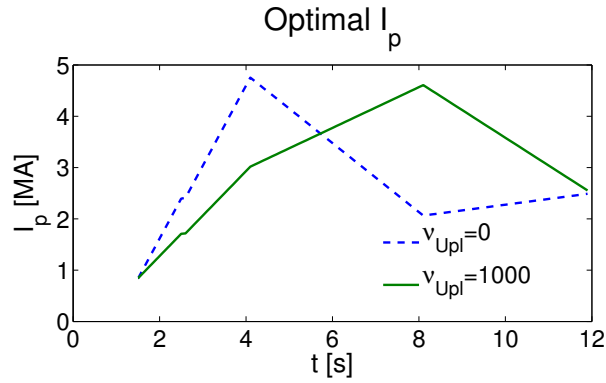


Figure 4.1: The contours of the two cost function terms considered, with the highest value of each term in red and the lowest in blue. The white area is inaccessible; the simulation crashes at those parameter values (see Sec. 4.2.1).



(a) Contours of $J_{U_{pl}}$ (black lines) and $J_{\Psi_{OH}}$ (colour) overlaid with minima of J (Eq. (4.8)) for different values of $\nu_{U_{pl}}$.



(b) The I_p trajectories corresponding to the two most extreme points of (a).

Figure 4.2: Results of unconstrained optimization of J .

4.2 Constraints

Although unconstrained optimization may yield interesting results, these are often unattainable in a tokamak or undesirable for reasons not considered in the optimization, e.g. stability considerations. It is thus necessary to constrain optimizations to keep them within physically acceptable limits. This section will address both constraints on the actuator trajectories and constraints on the plasma state itself.

Constraints on the trajectories are simple to implement, since `fmincon` accepts both equality and inequality constraints on the free parameters (see Sec. 2.6). The trajectory constraints at JET are given in Tab. 4.1. JET can deliver a total of 24 MW of NBI power, up to 12 MW per actuator in this model. To prevent shine-through¹, the neutral beams can only be engaged when the mean density \bar{n} is above $2 \times 10^{19} \text{ m}^{-3}$. Although the density is part of the plasma state, it is possible to implement the minimum density condition as a trajectory constraint here be-

Maximum current	$I_p \leq 5 \text{ MA}$
Minimum current	$I_p \geq 0.05 \text{ MA}$
Fastest current ramp	$\left \frac{dI_p}{dt} \right \leq 0.5 \text{ MA/s}$
Maximum NBI power per actuator	$P_{NBI} \leq 12 \text{ MW}$
NBI engaged only above minimum mean density	$P_{NBI}(t) = 0 \ \forall \ t$ such that $\bar{n}(t) \leq 2 \times 10^{19} \text{ m}^{-3}$
L-mode operation	$P_{NBI} \leq 5 \text{ MW}$
H-mode operation	$P_{NBI} \geq 5 \text{ MW}$

Table 4.1: The trajectory constraints at JET.

cause the density is prescribed for the duration of the shot. This allows the pre-selection of a time at which NBI power is first allowed. The auxiliary power threshold to induce L-H transition was taken to be 5 MW.

Constraints on the plasma state (which is described here by the quantity $x(t)$) are typically expressed in the form $c_i(t, x(t)) \leq 0$. However, this implies one constraint per time step used in the optimization, which is very inefficient. Instead, we integrate over time to get a more reasonable constraint expression:

$$\mathcal{C}_i = \left(\int_{t_0}^{t_f} [\max(0, c_i(t, x(t)))]^2 dt - \epsilon \right) \leq 0, \quad \epsilon > 0 \quad (4.9)$$

where ϵ is a small relaxation of the constraint (Felici, 2011). Now each condition can be simply described by one constraint $\mathcal{C}_i < 0$.

¹The minimum density allowed is specified in the JET Facility Operation Instructions and depends on e.g. the desired NBI pulse length and beam energy; the value given here is an average value for long NBI pulses and standard settings (G.M.D. Hogeweij, private communication, April 1, 2014).

The most important state constraint for this project is the constraint $q > q_{lim}$ (or equivalently, $\iota < \iota_{lim} = 1/q_{lim}$), which ensures that sawtooth action is eliminated. Following Felici (2011), we define $c_{\iota < \iota_{lim}}$ as

$$c_{\iota < \iota_{lim}}(t, x(t)) = \int_0^{\rho_{max}} \max(0, (\iota(\rho, t) - \iota_{lim})) d\rho \quad (4.10)$$

The state constraint is then given by

$$\mathcal{C}_{\iota < \iota_{lim}} = \left(\int_{t_0}^{t_f} c_{\iota < \iota_{lim}}(t, x(t))^2 dt - \epsilon \right) \leq 0 \quad (4.11)$$

It was not necessary to take the maximum in $\mathcal{C}_{\iota < \iota_{lim}}$ since $c_{\iota < \iota_{lim}}(t)$ was defined to be non-negative.

4.2.1 Constrained Optimization Example

The unconstrained optimization example in Sec. 4.1.1 was very unrealistic, even for modest constraints. To demonstrate the effects of both trajectory and state constraints, the trajectory constraints of Tab. 4.1 will now be enforced, along with requiring $q(\rho) > 0.95 \forall \rho$. It can be seen directly from the axes of Fig. 4.2 where the trajectory constraints are violated. From Eq. (4.7), the plasma current was fixed at 0.85 MA at $t = 1.5$ s. Since $|dI_p/dt| \leq 0.5$ MA/s, it is clear that I_{p1} (at 4.0 s), cannot exceed 2.1 MA. Similar reasoning yields that $I_{p2} \leq 4.5$ MA and $I_{p2} \leq (I_{p1} + 2 \text{ MA})$.

The state constraint, by contrast, is completely unclear from the figures pre-

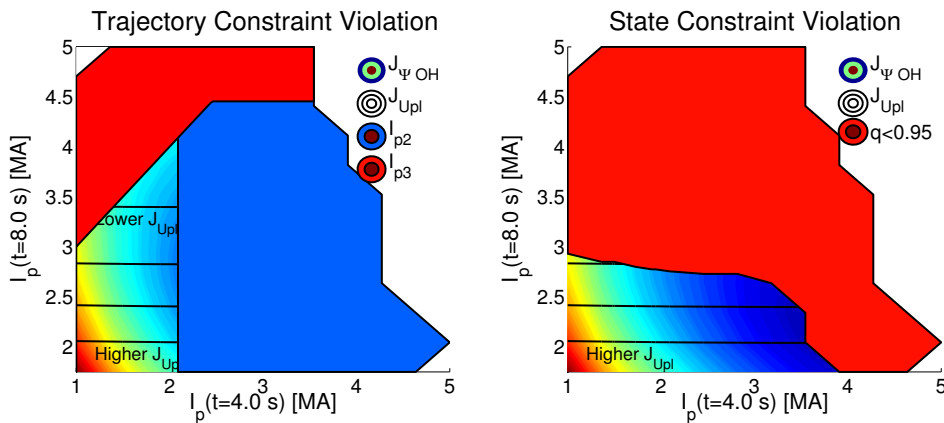
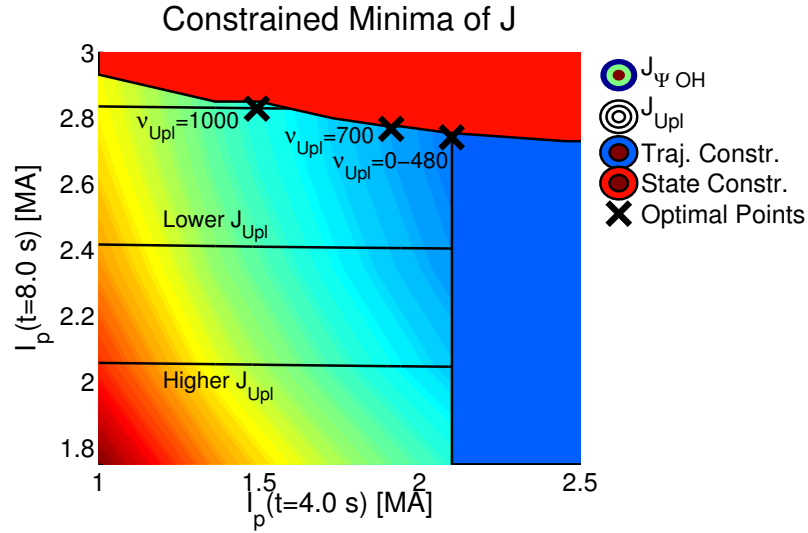


Figure 4.3: The parameter space of Sec. 4.1.1, with contours of $J_{\Psi_{OH}}$ (blue low, red high) and J_{Upl} (black lines, higher at bottom of figure). **Left:** Areas in which the trajectory constraints of Tab. 4.1 are violated. Violations of the I_{p1} maximum are shown in blue, and violations of the I_{p2} constraints are shown in red (see text). **Right:** Areas in which the state constraint $q > 0.95$ is violated.

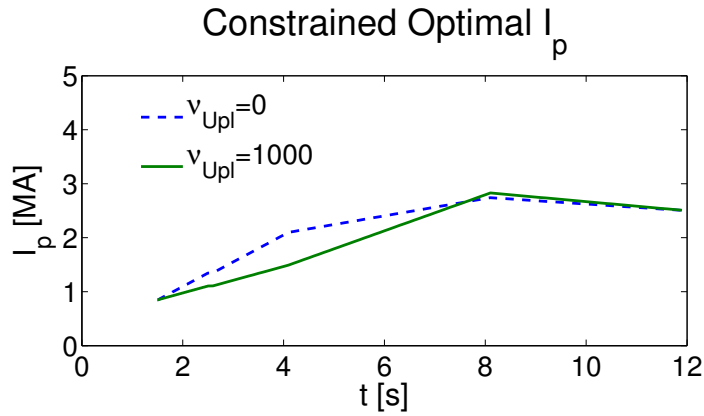
sented so far. A simulation must be run at each of the scanned points in parameter space to determine whether or not the constraint is violated. The results of these simulations are presented in Fig. 4.3. All the optimal points found in the unconstrained example are not only undesirable, they are unattainable at JET. The inaccessible white-space, where the simulation crashed, is far outside the boundaries of what JET could ever achieve, so instability of the software there is not a concern.

Performing optimizations of J (Eq. (4.8)), with $\nu_{U_{pl}}$ ranging from 0 (low importance of $J_{U_{pl}}$) to 1000 (high importance) and including constraints, yields the results in Fig. 4.4a. For $\nu_{U_{pl}} \leq 480$, the effects of the constraints are clearly visible: all of these variations of the cost function yield the same minimum, which sits at the edge of constraint violation. We say that the constraints are **active** here. These points correspond to trajectories which ramp the plasma current at the maximum rate possible, and which produce a plasma with a minimum q approaching 0.95.

For $\nu_{U_{pl}} = 700$ and 1000, the minimum begins to depart from the earlier points. These very high weights of $J_{U_{pl}}$ attract the minimum upwards strongly enough to begin moving along the border of the region violating $q > 0.95$. At these points, the trajectory constraints are no longer active, only the state constraint. The corresponding trajectories do not push JET's current ramp limits, but they do have minimum q values approaching 0.95.



(a) Contours of $J_{\Psi OH}$ (colour) and J_{Upl} (black lines) overlaid with constrained minima of J (Eq. (4.8)) for different values of ν_{Upl} . Also shown are the areas of trajectory constraint violation (blue) and state constraint violation (red).



(b) The I_p trajectories corresponding to the two most extreme points of (a).

Figure 4.4: Results of constrained optimization of J . For $0 \leq \nu_{Upl} \leq 480$ the constrained minima all corresponded to the same trajectory.

4.3 Time Knots and Sensitivity

One of the major concerns when performing an optimization is the existence of local minima in the cost function. With such a complex problem some local minima presumably exist in which the optimization may become ‘trapped’. To lower the chances of this situation occurring, we will follow the procedure of Van Dongen (2013), increasing the number of free parameters (time knots) per trajectory. Each consecutive set of knots will contain the previous set, so that if the previous trajectory was indeed optimal, then the next trajectory has the option to return to that case.

Increasing the number of free parameters (n_f) has the effect of changing the sensitivity of the optimal trajectory to the transport model used. Since models are never exact, it is important that a small perturbation in the model produces a small change in the discovered optimal trajectory. To probe this effect, we will optimize the cost function

$$J = J_{s/q} + \nu_{ss} J_{ss} \quad (4.12)$$

for $\nu_{ss} = 5 \times 10^6$. For each n_f the sensitivity to the model is probed by perturbing the Bohm/gyro-Bohm transport model coefficients (see Sec. 2.3) by a factor:

$$\begin{pmatrix} c_{e,b}^{\text{pert}} \\ c_{e,gb}^{\text{pert}} \end{pmatrix} = C_{\text{pert}} \times \begin{pmatrix} c_{e,b} \\ c_{e,gb} \end{pmatrix}, \quad 0.9 \leq C_{\text{pert}} \leq 1.1 \quad (4.13)$$

The cost-function is then re-calculated using various values of C_{pert} . The spread of these points is an indication of the sensitivity of the optimization to the specific model used.

It was expected that a more complex problem would result in optimal trajectories which were more sensitive to initial conditions; to explore the ‘worst-case’ (most sensitive) scenario as an example, the analysis was performed on an optimization of the H-mode ramp-up. Recall from Sec. 3.3 that this ramp-up has three actuator trajectories: the plasma current, and both on- and off-axis NBI power.

Taking into account the error analysis of the trajectories in Fig. 3.3 and 3.5 (reproduced in Fig. 4.6), in particular the divergence of the CRONOS and RAPTOR temperature profiles after the last NBI power step at 11.0 s, the last part of the trajectory was discarded. All H-mode optimizations will thus run from 1.5 s to 11.0 s after plasma breakdown. It is clear from the large steps in the NBI trajectories that at least 4 time knots will be required: 1.5 s (the initial time), 4.0 s (first NBI step), 8.1 s (second NBI step), and 11.0 s (final time), so $n_f \geq 4$. The

additional time knots were added in the following sequence:

$$t_{add}[s] = [6.0, 10.0, 9.0, 5.0, 7.0, 2.75] \quad (4.14)$$

The results of the perturbations are displayed in Fig. 4.5, along with the relative spread, defined by

$$\text{Relative Spread} = \frac{\text{std}(J)}{|J_0|} \quad (4.15)$$

where $\text{std}(x)$ is the standard deviation of x and J_0 the unperturbed J value obtained from optimization. It is clear that the optimal choice in this case is 6 time knots:

$$t_{knots}[s] = [1.5, 4, 6, 8.1, 10, 11] \quad (4.16)$$

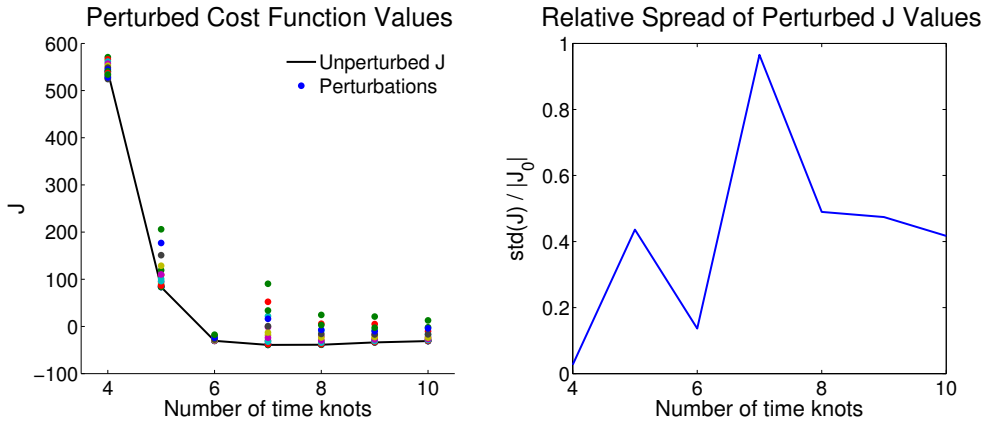


Figure 4.5: Post-optimization cost function values for a perturbed transport model (see text for specific time knots used in each case). In this case, 6 time knots resulted in a low optimized J value and a low relative spread.

4.4 Results and Discussion

A sample of full optimizations will be presented. The cost functions explored are not exhaustive, however the method is easily adapted to any cost function which may be desired at a later time. The first optimization will be based on the H-mode shot 83224 and the optimization process will be explained in detail. By way of comparison, a similar optimization will then be discussed for the L-mode (shot 83223) case.

4.4.1 Stationary State vs. s/q in H-mode

In this section an optimization of the stationary state condition (flat U_{pl} profile) and s/q will be explored. The same cost function as in the sensitivity analysis of the

previous section (Eq. (4.12)) will be used with $\nu_{ss} \in \{0, 10^1, 10^2, 10^3, 10^4, 10^5\}$, such that J ranges from pure $J_{s/q}$ to domination by J_{ss} .

As the nominal case, the trajectories of JET shot 83224, used in the H-mode benchmark (Sec. 3.3), were used as a basis for piecewise-defined nominal trajectories with the appropriate time knots. The plasma current was chosen to be piecewise linear, and the NBI powers piecewise constant. Least squares fitting led to the nominal trajectories in Fig. 4.6.

Examining each term in the cost function after optimization in Fig. 4.7, it is clear why such a wide range of ν_{ss} values was needed: with respect to ν_{ss} , $J_{s/q}$ changes at a comparable rate to the *logarithm* of J_{ss} . The profiles corresponding to these J values are displayed in Fig. 4.8. As expected, the pure $J_{s/q}$ case resulted in a low, broad q profile, and therefore, more visibly, a high, broad ι profile (recall $\iota \equiv 1/q$). It can be seen that this came at the expense of stationarity: the U_{pl} profile varies greatly in ρ . However, a significant degree of stationarity can be recovered with even a modest ($\nu_{ss} = 100$) inclusion of J_{ss} in the cost function without completely sacrificing the broad q profile. Indeed, even when the primary goal of the optimization is stationarity, a significant improvement in s/q can be achieved over the nominal case.

The trajectories which produced the optimized profiles are displayed in Fig. 4.9 and 4.10. Intuitively, the intermediate ($\nu_{ss} = 100$) case falls between the two extreme cases in the I_p and total P_{NBI} trajectories. A large current overshoot coupled with high final P_{NBI} appears to maximize s/q , with these features becoming increasingly moderate as J_{ss} gains importance. However, the intermediate case does not fall between the two extremes for the individual NBI trajectories. Here the only obvious pattern appears to be an increasingly off-axis NBI source towards

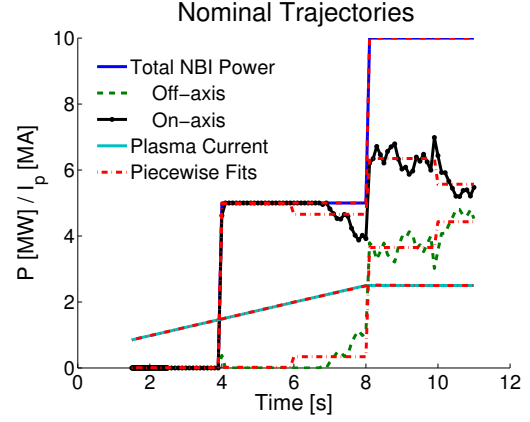


Figure 4.6: Piecewise fitting of the nominal trajectories. I_p was taken to be piecewise linear, and NBI powers piecewise constant.

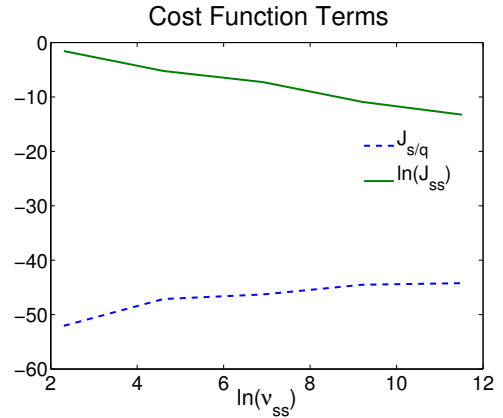


Figure 4.7: The terms in the cost function after optimization for all $\nu_{ss} \neq 0$. Note that the x-axis and the green line are both logarithmic, but $J_{s/q}$ is not.

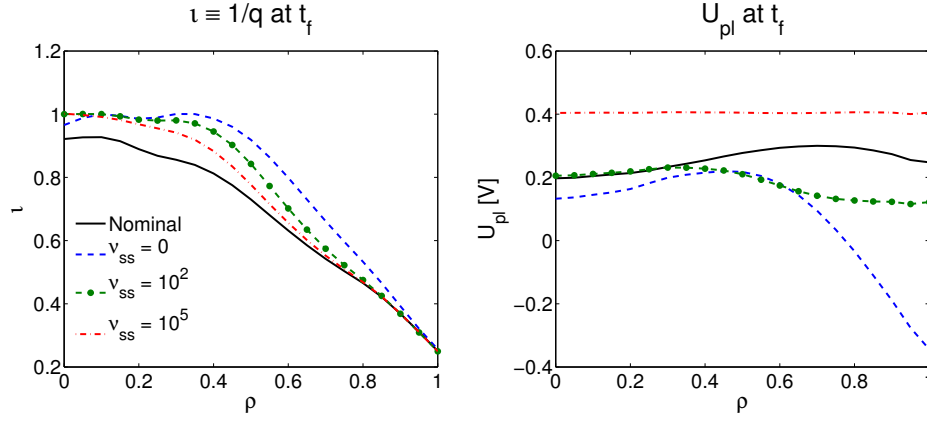


Figure 4.8: Resultant profiles at the final time for a selection of ν_{ss} values. Instead of q , ι is plotted to emphasize the differences between cases. Nominal case corresponds to trajectories in Fig. 4.6, optimized cases to Fig. 4.9 and 4.10.

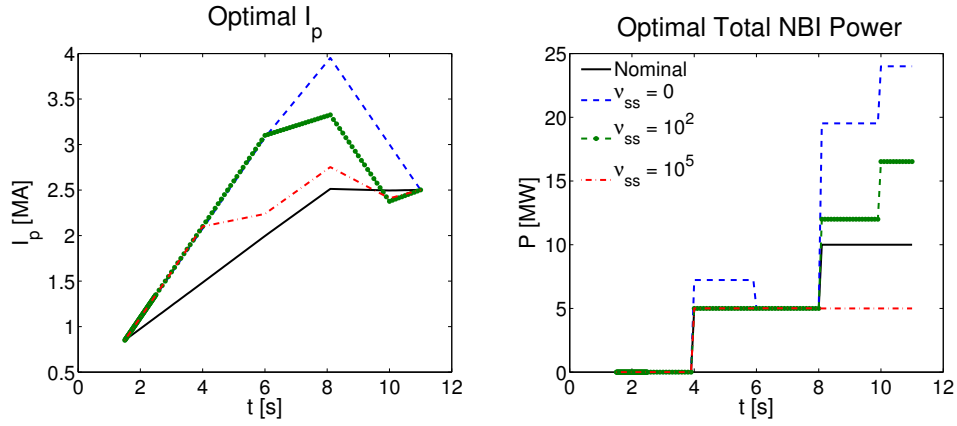


Figure 4.9: Optimized Trajectories. The intermediate ($\nu_{ss} = 100$) falls between the two extremes for I_p and for the total NBI power. The L-H transition (requiring at least 5 MW total NBI power) was at 4.0 s.

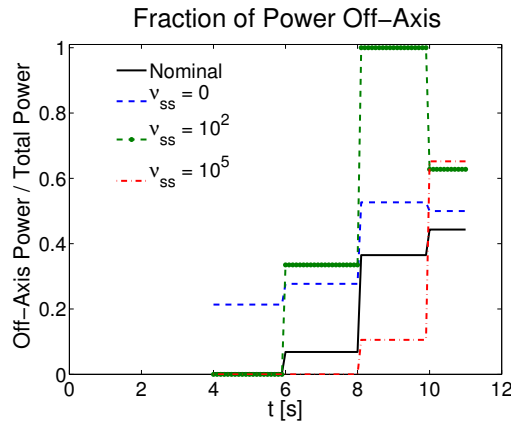


Figure 4.10: Proportion of off-axis power used in Fig. 4.9. Here $\nu_{ss} = 100$ does not fall between the two extreme cases. Note that these curves only begin at $t = 4.0$ s since before that time $P_{NBI} = 0$.

the end of the ramp-up for both optimization goals. This apparent lack of pattern may suggest some degeneracy in the trajectory parameter space, i.e. more than one set of trajectories may exist which will produce a similarly optimal result. The design of `fmincon` allows for the visual tracking of the optimization process, and for $\nu_{ss} \geq 100$ the optimization did not find an actual minimum, instead probing a variety of trajectories which produced very similar cost function values. The fact that this is possible further suggests some sort of degeneracy.

The additional freedom provided by this degeneracy suggests the possibility of minimizing an additional cost function term without significantly altering the values of the previously optimized terms. A good candidate term to add would be ohmic flux consumption, such that the optimized conditions could be maintained for longer during the flattop phase. This optimization has not yet been carried out due to time constraints.

4.4.2 Stationary State vs. s/q in L-mode

To enable comparison, the stationarity vs. s/q cost function will also be optimized in L-mode, using JET shot 83223 from Sec. 3.2 as the nominal case. This shot relied purely on ohmic heating, using only the I_p trajectory from Fig. 4.6. However, it was found that in L-mode, pure ohmic heating was incapable of satisfying the $q > 1$ constraint within the operational limits imposed by the trajectory constraints in Tab. 4.1 (though $q > 0.95$ was found to be feasible in Sec. 4.2.1). This effect is of course cost function independent. To overcome this, some freedom in the NBI power was introduced into the optimization: instead of requiring $P_{NBI} = 0$, the less restrictive constraint $P_{NBI} \leq 5$ MW was imposed. This keeps the total NBI power below the assumed L-H transition threshold power, validating the choice to keep the simulation in L-mode.

The cost function weights explored were the same as those in the H-mode case of Sec. 4.4.1. Optimization results are displayed in Fig. 4.11 - 4.13. Compared to the H-mode case, it is clear that in L-mode the results are less optimal: the ι profiles are lower and narrower, and the U_{pl} profiles are less flat. In fact, for $\nu_{ss} > 10$, the overall results are actually *worse* than the nominal case. This is because of the $q > 1$ constraint, the satisfaction of which takes priority over optimization. Since the nominal case violated this constraint (the nominal ι profile in Fig. 4.11 is visibly higher than 1), the obtained results are more stable, but less optimal as determined by the cost function.

In the optimized trajectories, an overshoot is again observed to improve confinement via s/q . There does not appear to be a clear trend in the NBI trajectories, other than off-axis power being heavily favoured. The favouring of off-axis power

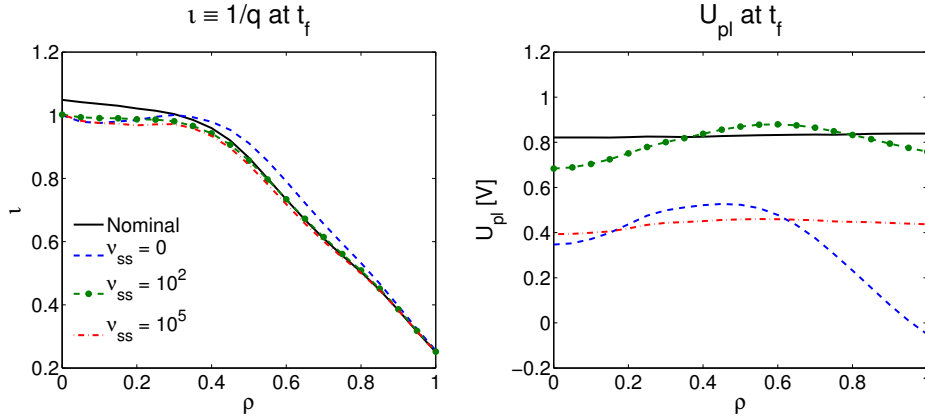


Figure 4.11: Resultant profiles at the final time for a selection of ν_{ss} values. Nominal case corresponds to I_p trajectory in Fig. 4.6, and zero NBI power. Optimized cases correspond to to Fig. 4.12 and 4.13.

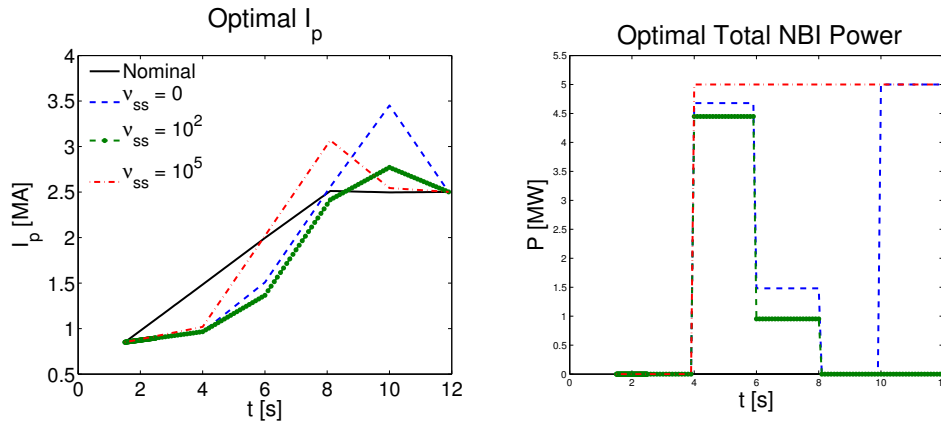


Figure 4.12: Optimized Trajectories. The intermediate ($\nu_{ss} = 100$) case is not in general between the two extremes for either I_p or P_{NBI} .

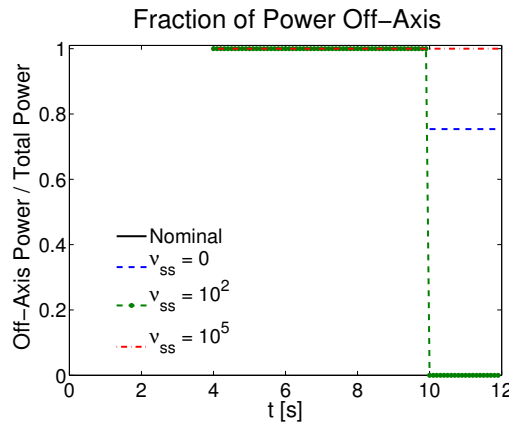


Figure 4.13: Proportion of off-axis power used in Fig. 4.9. Again, $\nu_{ss} = 100$ does not fall between the two extreme cases. Note that these curves only begin at $t = 4.0$ s since before that time $P_{NBI} = 0$.

is likely influenced by the $q > 1$ constraint. Since the neutral beam systems also drive some current (see Fig. 3.2), these optimizations seem to be using the NBI to drive more off-axis current. The lower current density in the centre of the plasma leads to a higher q there, helping to satisfy the constraint.

It is again observed that some degeneracy may exist, as the intermediate $\nu_{ss} = 100$ trajectory falls outside of the two extreme cases. In these results, this effect is observed in all 3 of the trajectories.

5 Conclusion

The manner in which a plasma is heated during the ramp-up phase of a tokamak discharge can have effects lasting long into the shot. Heating actuators, whose trajectories are typically simply chosen by operators, can help to improve the conditions for fusion in a tokamak, with this project focusing on JET. Instead of expensive experiments, various actuator trajectories are explored via numerical optimization.

The option of using automated optimization techniques on tokamak discharge simulations has only recently become available thanks to the new, high speed RAPid Plasma Transport simulatOR (RAPTOR). RAPTOR's high speed makes the simulation of hundreds of ramp-ups with similar trajectories feasible, at the cost of decreased accuracy. To ensure that optimization would produce meaningful results, RAPTOR simulations are first benchmarked against similar simulations from the more complete CRONOS suite of codes.

Analysis of the simulation in Chap. 3 results reveals good agreement between RAPTOR and CRONOS for the majority of the simulation in both L-mode (utilizing only ohmic heating via the plasma current) and H-mode (which additionally includes neutral beam heating). One notable difference between the outcomes is the enhanced flattening of RAPTOR's loop voltage profiles at the end of the ramp-up. Since this behaviour is to be expected, it is concluded that this is more likely an issue in CRONOS than in RAPTOR, and thus the RAPTOR model is deemed sufficient to produce meaningful results. This result lends confidence to the quality of RAPTOR's actuator simulation and the validity of its underlying assumptions.

Optimization is performed by defining a cost function, which evaluates the plasma state after the ramp-up for a given set of actuator trajectories. By making small changes to the trajectories and iterating, moving towards a minimum of the cost-function, the automated SQP optimization routine in MATLAB seeks out the best trajectories. Cost function terms are defined in Sec. 4.1 to seek out a stationary or even steady state, improve confinement by influencing Ion Temperature Gradient driven turbulence, or minimize ohmic flux consumption.

Constraints to the optimization are implemented in two ways in Sec. 4.2. The first is direct constraints on the trajectories based on operational limits of JET,

including limits on the plasma current and its rate of change, maximal NBI power, minimum density to prevent NBI shine-through, and the requirement to stay above or below the L-H transition power threshold. The state of the plasma itself may also be constrained, in particular by requiring the safety factor to remain above 1 to avoid the sawtooth instability. Time knots for the optimization are chosen in Sec. 4.3 to minimize dependence on the semi-empirical transport model while still achieving significant improvement in the cost-function.

Optimization of a two-term cost function seeking out improved confinement and stationarity with varying degrees of relative importance is carried out in Sec. 4.4. In H-mode, a large current overshoot and high NBI power is observed to improve confinement, while stationarity requires more moderation in these trajectories. Similar results for the plasma current are obtained in L-mode, but the NBI power usage shifts to focusing on maintaining $q > 1$ via the NBI off-axis current drive. In both cases, some degeneracy in trajectory space is observed: optimized trajectories for intermediate importance of the cost function terms do not simply fall between the results for cost functions where one term dominates, suggesting that there are multiple trajectories which can produce similar results. This implies that more cost function terms could be added to exploit this extra freedom, though this work has not yet been carried out.

The success of this automated optimization method in discovering actuator trajectories which result in more ideal plasmas within given constraints suggests a bright outlook for this new area of research. The efficiency of the technique – one optimization typically takes less than 10 minutes on a standard laptop – makes it an ideal way to discover new trajectories which tokamak operators may not think of manually. To further explore the possibility of this becoming a more widely adopted technique, the results of RAPTOR simulations should be tested for validity, first by inputting the optimal trajectories into a more complete simulation like CRONOS, and then, assuming that the improvements are maintained, by testing the new trajectories on JET itself. With this added experimental validation, it would not be hard to imagine helping to meet future plasma requirements for fusion using an automated optimization method.

References

- Artaud, J., Basiuk, V., Imbeaux, F., Schneider, M., Garcia, J., Giruzzi, G., et al. (2010, April). The CRONOS suite of codes for integrated tokamak modelling. *Nuclear Fusion*, 50(4), 043001. Available from <http://stacks.iop.org/0029-5515/50/i=4/a=043001?key=crossref.789a86752c1e600c667a9bacdac4c6e9>
- Citrin, J., Artaud, J. F., Garcia, J., Hogeweij, G. M. D., & Imbeaux, F. (2010, November). Impact of heating and current drive mix on the ITER hybrid scenario. *Nuclear Fusion*, 50(11), 115007. Available from <http://iopscience.iop.org/0029-5515/50/11/115007>
- EFDA. (2014a). *FAQs*. Available from <http://www.efda.org/faqs/>
- EFDA. (2014b). *Tokamaks*. Available from <http://www.efda.org/fusion/fusion-machine/types-of-fusion-machines/tokamaks/>
- Erba, M., Aniel, T., Basiuk, V., Becoulet, A., & Litaudon, X. (1998, July). Validation of a new mixed bohm/gyro-bohm model for electron and ion heat transport against the ITER, tore supra and START database discharges. *Nuclear Fusion*, 38(7), 1013–1028. Available from http://iopscience.iop.org/0029-5515/38/7/305/pdf/0029-5515_38_7_305.pdf
- Erba, M., Cherubini, A., Parail, V. V., Springmann, E., & Taroni, A. (1997, February). Development of a non-local model for tokamak heat transport in l-mode, h-mode and transient regimes. *Plasma Physics and Controlled Fusion*, 39(2), 261–276. Available from http://iopscience.iop.org/0741-3335/39/2/004/pdf/0741-3335_39_2_004.pdf
- EURATOM, & CCFE. (2013). *Annual report of the EURATOM/UKAEA fusion programme 2012/13* (Tech. Rep.). Culham, UK. Available from http://www.ccfe.ac.uk/annual_reports.aspx#1213
- Felici, F. (2011). *Real-time control of tokamak plasmas: from control of physics to physics-based control*. PhD thesis no.5203, École Polytechnique Fédérale de Lau-

- sanne (EPFL), Lausanne. Available from <http://library.epfl.ch/theses/?nr=5203>
- Felici, F., & Sauter, O. (2012, February). Non-linear model-based optimization of actuator trajectories for tokamak plasma profile control. *Plasma Physics and Controlled Fusion*, 54(2), 025002. Available from <http://stacks.iop.org/0741-3335/54/i=2/a=025002?key=crossref.7771d3637a1052accfa9dff36ffbb072>
- Freidberg, J. P. (2007). *Plasma physics and fusion energy*. Cambridge: Cambridge University Press. Available from <http://public.eblib.com/EBLPublic/PublicView.do?ptiID=288647>
- FuseNet. (2011, July). *Pedestal*. Available from <http://wiki.fusenet.eu/wiki/Pedestal>
- Hender, T., Wesley, J., Bialek, J., Bondeson, A., Boozer, A., Buttery, R., et al. (2007, June). Chapter 3: MHD stability, operational limits and disruptions. *Nuclear Fusion*, 47(6), S128–S202. Available from <http://stacks.iop.org/0029-5515/47/i=6/a=S03?key=crossref.0b9322e42a59b955269531e35f39b3bb>
- Lütjens, H., Bondeson, A., & Sauter, O. (1996, September). The CHEASE code for toroidal MHD equilibria. *Computer Physics Communications*, 97(3), 219–260. Available from <http://linkinghub.elsevier.com/retrieve/pii/001046559600046X>
- Nocedal, J. (2006). *Numerical optimization* (2nd ed.). New York: Springer.
- Shimada, M., Campbell, D., Mukhovatov, V., Fujiwara, M., Kirneva, N., Lackner, K., et al. (2007, June). Chapter 1: Overview and summary. *Nuclear Fusion*, 47(6), S1–S17.
- Van Dongen, J. (2013). *Optimization of hybrid scenario ITER ramp-up*. Master thesis, Universiteit Utrecht, Utrecht. Available from <http://dspace.library.uu.nl/handle/1874/280138>
- Wagner, F. (2007, December). A quarter-century of h-mode studies. *Plasma Physics and Controlled Fusion*, 49(12B), B1–B33. Available from <http://stacks.iop.org/0741-3335/49/i=12B/a=S01?key=crossref.4b1659cd2933e3e40b713717cd852006>
- Wesson, J. (2004). *Tokamaks* (3rd ed.) (No. 118). Oxford: Oxford University Press.